A Zirconium Photosensitizer with a Long-Lived Excited State: Mechanistic Insight into Photo-Induced Single Electron Transfer

Yu Zhang, Tia S. Lee, Jeffrey L. Petersen, and Carsten Milsmann

J. Am. Chem. Soc., **Just Accepted Manuscript** • Publication Date (Web): 19 Apr 2018

A Zirconium Photosensitizer with a Long-Lived Excited State: Mechanistic Insight into Photo-Induced Single Electron Transfer.

Yu Zhang,[†] Tia S. Lee,[‡] Jeffrey L. Petersen,[†] and Carsten Milsmann[†]*

[†] *C. Eugene Bennett Department of Chemistry, West Virginia University, Morgantown, West Virginia 26506, United States*

[‡] *Department of Chemistry, Princeton University, Princeton, New Jersey 08544, United States*

camilsmann@mail.wvu.edu

Abstract

Time-resolved emission spectroscopy for the luminescent zirconium complex $Zr(^{Me}PDP)_2$ (^{Me}PDP = 2,6-bis(5-methyl-3-phenyl-1H-pyrrol-2-yl)pyridine) revealed a long-lived excited state with a lifetime τ = 325 ± 10 μs. Computational studies using time-dependent density functional theory (TD-DFT) were conducted to identify the nature of the luminescent excited state as a mixed triplet intraligand/ligand-to-metal charge transfer (^{3}IL/^{3}LMCT) state. Stern-Volmer experiments showed a strong dependence of the quenching rate on the redox potential of the quencher indicating photo-induced single electron transfer (SET) as the quenching pathway. Mechanistic investigations of the photocatalytic homocoupling of benzyl bromide allowed the detection of organic radical intermediates during turnover and provided further evidence for SET mediated by $Zr(^{Me}PDP)_2$. Isolation of the one-electron reduced form of the photosensitizer, $[Zr(^{Me}PDP)_2]^{1-}$, enabled studies of its electronic structure by a combination of experimental and computational techniques and confirmed its role as a strong reductant. Additionally, the role of the benzimidazolium hydride derivatives (^{R}BIH) as two-electron sacrificial reductants during photoredox catalysis was investigated. In combination, the results presented in this report

establish a detailed mechanistic picture of a photoredoxcatalytic reaction promoted by an earth-abundant early transition metal photosensitizer.

Introduction

Replacing precious metal catalysts with complexes based on earth-abundant metals is an attractive goal considering the economic and environmental benefits resulting from the lower costs and reduced toxicity of these elements, respectively. For traditional organometallic applications such as polymerization,[1,2] olefin functionalization,[3–7] cross-coupling,[8–12] or C-H functionalization,[13–16] significant advancements in base metal catalysis have been reported over the last decades. In contrast, photochemical and photovoltaic applications relying on the use of molecular transition metal photosensitizers are still dominated by precious metal complexes with derivatives of $[Ru(bpy)_3]^{2+}$ (bpy = 2,2'-bipyridine),[17–20] $[Ir(ppy)_3]$ (ppy = 2-phenylpyridine),[21,22] and $[ReCl(CO)_3(bpy)]$[23,24] as the most prominent examples. While the design of photoactive coordination compounds from earth-abundant metals has been a long-standing target,[25,26] further urgency has been added by the increasing demand for efficient solar energy conversion[27–29] and the rise of photoredox catalysis as a rapidly expanding field in organic synthesis.[30–35] The production of solar fuels and photovoltaic applications on a global scale in particular are limited by the low abundance of traditional molecular photosensitizers materials.[36,37]

The popularity of precious metal photosensitizers can be attributed to their favorable and well-understood photochemical and electron transfer properties: Efficient light absorption in the visible region of the spectrum via metal-to-ligand charge transfer (MLCT) from an electron rich metal center (d^6, d^8, d^{10} electron configurations) to a π accepting ligand; facile intersystem crossing (ISC) to a long-lived excited state due to strong spin-orbit coupling in second- or third-row metals; reversible outer-sphere electron transfer in both excited state and ground state.[38] The

most critical obstacle in transferring these design principles to analogous complexes of the more abundant first-row transition metals, such as $[Fe(bpy)_3]^{2+}$ and related polypyridyl complexes, is the lower ligand field splitting in first-row metals compared to their precious metal congeners.[39,40] The resulting low-lying d-d excited states provide readily available non-radiative deactivation pathways and result in drastically decreased excited state lifetimes in the picosecond range.[41–43] One exception to this phenomenon are Cu^I diimine complexes that have gained increased attention over the last years.[44–50] These complexes possess d^{10} configurations that preclude ligand field excited states and allow excited state lifetimes in the photocatalytically useful nano- to microsecond range. A second class of MLCT photosensitizers avoiding the use of precious metals are isocyanide complexes of Cr^0, Mo^0, and W^0.[51–55] Despite significant advances in recent years, several challenges remain for this class of photosensitizers. While the high reducing power of the excited states provides large driving forces for excited state electron transfer, the molecules are easily oxidized in their ground state resulting in undesired side reactions. Additionally, the highest quantum yields and longest excited state lifetimes are observed for W, the element with the lowest abundance among the group VI elements.

In pronounced contrast to MLCT photosensitizers, luminescent metal complexes relying on alternative mechanisms for light absorption such as ligand-to-metal charge transfer (LMCT), ligand-to-ligand charge transfer (LLCT), or metal-centered excitations (i.e. d-d, f-f, or d-f) are not as well-studied, but offer the potential to expand the palette of metals suitable for photosensitizer development.[56] Recent reports of organic photoredox reactions using photoluminescent lanthanide complexes highlight the potential of "non-traditional" metals for the design of photosensitizers.[57–64] Early transition metals from groups III-V are particularly attractive targets for the development of non-precious metal photocatalysts due to their increased

abundance in the Earth's crust compared to most late transition metals and lanthanides. Among these relatively earth-abundant elements, titanium and zirconium occupy a prominent position as the second and fourth most abundant among all transition metals, respectively.[36,37] The electron-deficient nature of these species requires a reversal of the charge-separation step upon light absorption from MLCT to ligand-to-metal charge transfer (LMCT). The readily accessible d^0 electron configuration commonly found for early transition metals prevents detrimental ligand field deactivation pathways and allows for extended luminescence lifetimes. Prompted by the initial discovery of long-lived luminescent LMCT states in cyclopentadienyl Sc^{III} complexes,[65,66] several examples of luminescent group III-V metal complexes with d^0 configuration have been reported.[67–77] However, most of these complexes do not exhibit reversible redox properties and often require excitation by UV light. In contrast, we recently reported the synthesis of the zirconium complex, $Zr(^{Me}PDP)_2$ ($H_2{}^{Me}PDP$ = 2,6□bis(5□methyl□3□phenyl□1H□pyrrol□2□yl)-pyridine), that shows photoluminescence upon visible light excitation and can undergo reversible electron transfer in the ground state.[78] This report also demonstrated the utility of $Zr(^{Me}PDP)_2$ as a photosensitizer in visible light promoted, reductive photoredox reactions previously performed using precious metal catalysts. While these studies provided a proof of concept for photocatalysis by group IV metal complexes, the mechanistic details of the photocatalytic reactions as well as several key properties of $Zr(^{Me}PDP)_2$ such as the exact nature of the emission (phosphorescence vs. fluorescence) and the lifetime of the luminescent excited state remained unclear.

Herein, we report a detailed mechanistic study into photo-induced single-electron transfer (SET) by $Zr(^{Me}PDP)_2$ and provide further insight into the excited state properties of the complex. The previously reported reductive homocoupling reaction of benzyl bromide to bibenzyl was

chosen as a model system to firmly establish SET reactivity rather than energy transfer pathways via in-situ trapping and characterization of radical intermediates. Isolation and characterization of the one-electron reduced form of the zirconium photosensitizer provide further insight into the electron transfer characteristics of $Zr(^{Me}PDP)_2$.

Results and Discussion

Re-Evaluation of the Photocatalytic Model System. To establish a reliable protocol for the mechanistic investigation of photo-induced SET by $Zr(^{Me}PDP)_2$, our study commenced with a re-evaluation of the reaction conditions for the photoredox catalytic reductive homocoupling of benzyl bromide (Table 1). As previously demonstrated, this reaction can be conducted under irradiation with commercially available green LEDs (λ_{max} = 520 nm) using $Zr(^{Me}PDP)_2$ as the photosensitizer, 1,3-dimethyl-2-phenyl-2,3-dihydro-1H-7-methylbenzo-[d]imidazole, ^{Me}BIH, as the sacrificial reductant, and 2,6-lutidine as the base. Control experiments conducted in the absence of light and/or $Zr(^{Me}PDP)_2$ resulted in quantitative recovery of starting materials, while reactions without addition of base resulted in low turnover and rapid catalyst decomposition.[78] One potential complication for a thorough mechanistic study under these initial conditions is the presence of benzylic C-H bonds in ^{Me}BIH which can undergo unwanted side reactions with benzyl radical intermediates in the proposed SET mechanism. This hypothesis is supported by the low yield of bibenzyl (30% at >99% conversion of benzyl bromide) and concomitant formation of ^{Me}BIH derived side products during photocatalytic turnover. The benzimidazolium hydride derivatives ^{H}BIH and ^{Cl}BIH studied previously provide more selective product formation, but result in slow photocatalytic reactions which can be attributed to their more positive redox potentials (Table 1, entries 2-4).

Building on these observations, ^{MeO}BIH – a more reducing BIH derivative without benzylic protons - was introduced for the present study to improve the selectivity and rate of the reaction. Despite an improved reaction time (Table 1, entry 5), the yield of bibenzyl was poor (19%) and a significant amount of toluene (15%) was observed as a by-product. This competing hydrodehalogenation reaction was proposed to result from facile hydrogen atom abstraction from the oxidized form of the sacrificial reductant, ^{MeO}BIH$^{\bullet+}$, which exhibits a very weak C-H bond (BDFE = 29.3 kcal mol^{-1})[79] that can easily be attacked by a potential benzyl radical intermediate. This reactivity highlights the complex proton-coupled electron-transfer (PCET) properties of ^{R}BIH derivatives[79] and prompted further studies of the influence of the base on the photocatalytic performance.

A significant improvement was achieved by changing the base from 2,6-lutidine to the stronger base triethylamine, NEt_3, increasing the yield of bibenzyl (64%) while simultaneously decreasing the amount of toluene (Table 1, entry 6). This improvement is consistent with more facile deprotonation of ^{MeO}BIH$^{\bullet+}$ by the stronger base NEt_3 resulting in the formation of the strong single electron reductant ^{MeO}BI$^{\bullet}$ and preventing hydrogen atom transfer (HAT). While the formation of toluene was suppressed, small amounts of the ammonium salt [BnNEt_3]Br resulting from nucleophilic attack of NEt_3 on benzyl bromide were detected as a new by-product. The use of the bulkier trialkylamine base *N,N*-diisopropylethylamine did not alleviate this issue but resulted in slightly lower yields of the desired homocoupling product. Unfortunately, the use of the even stronger base DBU resulted in rapid formation of ammonium salts via nucleophilic substitution and completely shut down the desired photocatalytic pathway.

Table 1. Optimization of the reaction conditions for the photoredox catalytic coupling of benzyl bromide with Zr(^{Me}PDP)$_2$ as the photosensitizer.

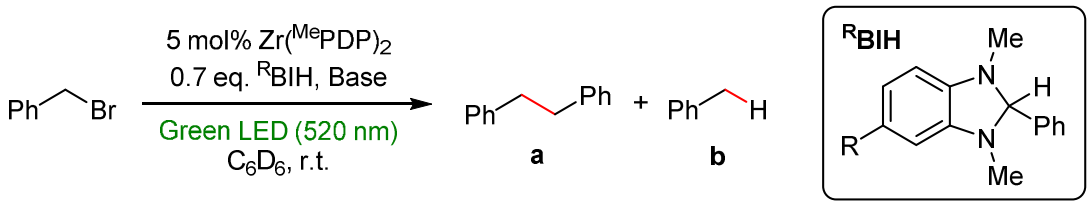

Entry	^{R}BIH	Base (equiv.)	pK_a of the base[a]	Time (h)	% Yield **a**/**b** (% Conv.)[b]
1[c]	^{Me}BIH	-	-	16	6:/ (47)
2[c]	^{Cl}BIH	2,6-lutidine (2.0)	14.13	108	29:/ (31)
3[c]	BIH	2,6-lutidine (2.0)	14.13	48	20:/ (21)
4[c]	^{Me}BIH	2,6-lutidine (2.0)	14.13	24	30:/ (99)
5	^{MeO}BIH	2,6-lutidine (2.0)	14.13	12	19:15 (100)
6[d]	**^{MeO}BIH**	**TEA (2.0)**	**18.82**	**12**	**64:10 (100)**
7[d]	^{MeO}BIH	DIPEA (2.0)	-	12	53:13 (100)
8[d]	^{MeO}BIH	DBU (2.0)	24.23	-	-
9[d]	^{MeO}BIH	TEA (10.0)	18.82	12	27:5 (100)

[a]pK_a value in MeCN from ref. [80]. [b] ^{1}H NMR yield and conversion of benzyl bromide using 1,3,5-trimethoxybenzene as the internal standard. [c]Data from ref. [78]. [d]Ammonium salts were formed.

Intermittent Illumination and Quantum Yield of Photocatalysis. With improved reaction conditions in hand, the photocatalytic nature of the reaction was initially investigated via an intermittent illumination experiment. A correlation of irradiation time and bibenzyl yield is shown in Figure 1. No product formation was observed in the absence of light which clearly establishes the light-dependent nature of the reaction. However, this type of experiment is not suitable to rigorously rule out a potential photo-initiated radical chain mechanism.[81] Even though it is difficult to envision such a pathway for the homocoupling reaction studied herein, the quantum yield of the reaction was determined via actinometry to provide further evidence for a photoredox catalytic mechanism. To establish the photon-flux of the illumination setup, the photodissociation of Reinecke's salt, $K[Cr(NH_3)_2(NCS)_4]$, was used as the chemical actinometer

due to its well-established quantum yield at 520 nm. The overall quantum yield of the photo reaction, Φ_{cat}, was then determined by dividing the number of product molecules formed by the number of photons absorbed over the illumination period (see Supporting Information for details). The low value of $\Phi_{cat} = 0.004$ obtained in this way for bibenzyl formation clearly favors a photoredox catalytic mechanism over a radical chain process. The significantly lower reaction quantum yield compared to the luminescence quantum yield of 0.08 is likely due to back electron transfer from the reduced photocatalyst to $^{MeO}BIH^{\bullet+}$. This non-productive pathway should be enhanced under the reaction conditions, because the two ionic products of photo-induced SET ($^{MeO}BIH^{\bullet+}$ and $[Zr(^{Me}PDP)_2]^{1-}$) are likely to remain in close enough proximity for facile outer-sphere back electron transfer as ion-pair formation is favorable in the non-polar reaction medium benzene.

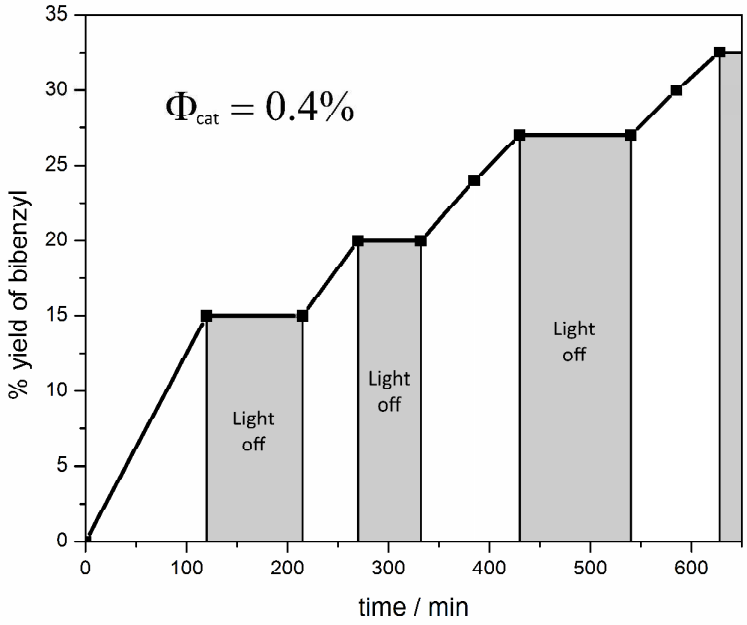

Figure 1. Intermittent illumination experiment for the photoredox catalytic homocoupling of benzyl bromide monitored by ^1H NMR in C_6D_6.

Excited State Lifetime and TD-DFT Studies. Our initial studies of the photoluminescence and electron transfer properties of $Zr(^{Me}PDP)_2$ did not investigate the emission lifetime or the multiplicity (singlet vs. triplet) of the excited state. To address these important questions, time-resolved emission data were collected for $Zr(^{Me}PDP)_2$. Excitation of the chromophore was performed at a wavelength of 516 nm, close to the absorption maximum in the visible region of the spectrum, and emission was detected at the maximum of the emission band at 595 nm for maximum signal intensity. A typical time-resolved emission trace for $Zr(^{Me}PDP)_2$ in rigorously deoxygenated and anhydrous THF solution at room temperature is shown in Figure 2and can readily be fit by a single exponential decay (see also Figure S9). Data collection and fits for multiple independently prepared samples yielded an excited state lifetime, τ_0, of 325 ± 10 μs for $Zr(^{Me}PDP)_2$ in THF. The strikingly long lifetime is indicative of phosphorescent emission due to a spin-forbidden $T_1 \rightarrow S_0$ transition. This result is also consistent with strong quenching of the emission in the presence of triplet O_2 (Figure S14). Phosphorescence lifetimes in the hundreds of μs range at room temperature are rare for transition metal complexes, but have been reported for d-d excited states (^2E_g) in $[Cr^{III}(phen)_3]^{3+}$ derivatives (phen = 1,10-phenanthroline)[82,83] and intra-ligand charge-transfer states (^{3}ILCT) in ZnTPP (TPP = tetraphenylporphyrin).[84]

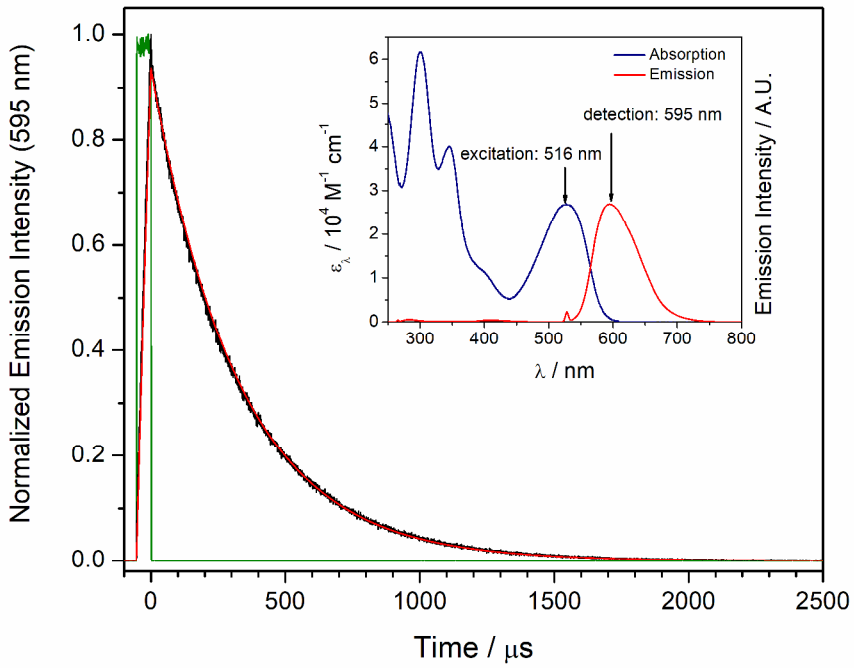

Figure 2. Time-resolved emission data for Zr(^{Me}PDP)$_2$ in THF at room temperature (black line) detected at 595 nm upon excitation at 516 nm (see inset). The red line shows the fit to a single exponential decay with τ_0 = 325 μs and the green trace shows the excitation pulse (516 nm).

The majority of phosphorescent transition metal complexes for photochemical applications relies on ^{3}MLCT excited states, which exhibit lifetimes in the ns to low μs range. In contrast, our previous computational analysis of the lowest energy absorption band of Zr(^{Me}PDP)$_2$ centered at 528 nm indicated that this feature is due to a transition with significant ligand-to-metal charge-transfer (LMCT) character.[78] With the results from time-resolved emission spectroscopy in hand, a more detailed analysis of the computational data obtained in these preliminary theoretical studies was conducted to further characterize the full UV/vis absorption profile of the complex and complement our initial report. Additional calculations of the electronic structure of the lowest energy triplet state were conducted to further investigate phosphorescent emission. The ground state (S_0) geometry of Zr(^{Me}PDP)$_2$ was obtained previously via geometry optimization and is in excellent agreement with the geometric parameters determined by single crystal X-ray diffraction (Table 3).[78] As is often seen in transition metal complexes, the metal ligand bond

distances in the computed structure are slightly overestimated by ca. 0.04 Å.[85] Even though no symmetry constraints were applied during optimization, the calculated structure exhibits D_{2d} local symmetry with two equivalent ^{Me}PDP ligands if the orientation of the phenyl substituents is disregarded. The maximum deviation for corresponding metal-ligand and intraligand bond distances between the two PDP moieties is 0.001 Å and the angle between the two ligand planes is 89.83°. The calculated absorption spectrum obtained via time-dependent density functional theory (TD-DFT) at the computed S_0 geometry is shown in Figure 3. For all TD-DFT calculations solvent effects were taken into account using the conductor-like screening model with parameters for THF.[86] The predicted spectrum is in good agreement with the experimental data showing four major absorption bands in the range of 285-1000 nm, which are labeled with Roman numerals in Figure 3. The most intense TD-DFT states (predicted oscillator strength $f_{osc} > 0.03$) contributing to these bands are labeled according to their state number. The transition energies and contributing single electron excitations (including their weight) for each TD-DFT state are given in Table 2.

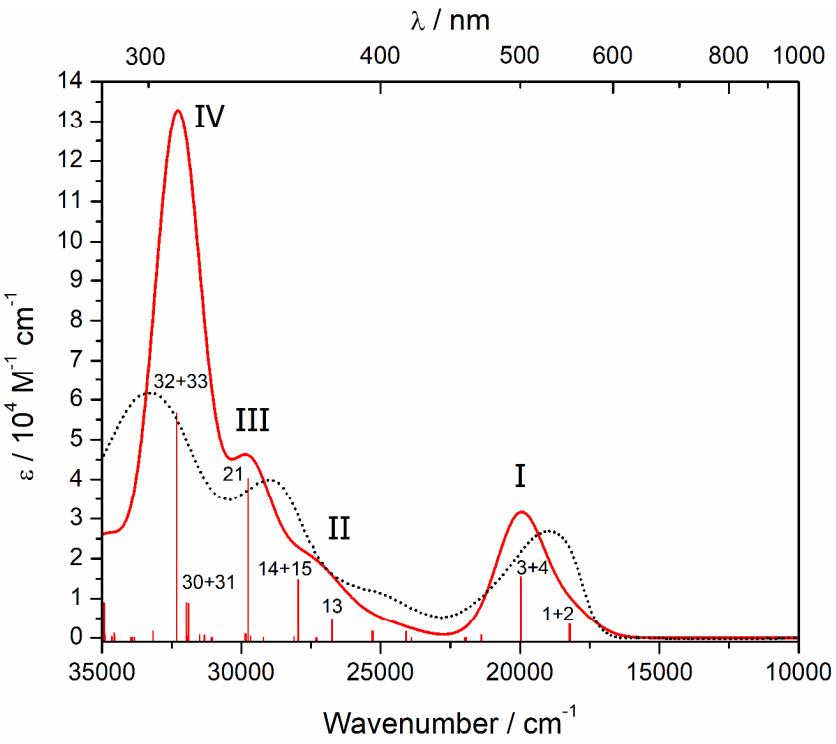

Figure 3. Electronic absorption spectrum of Zr(^{Me}PDP)$_2$ obtained via TD-DFT calculations (red line, FWHM of 2000 cm^{-1}). The stick plot indicates the positions and relative intensities of individual transitions. Transitions with calculated oscillator strengths larger than 0.03 are labeled according to their TD-DFT state number. The major contributions to each numbered state are listed in Table 2. The experimental spectrum is shown as a dotted black line for comparison.

Table 2. Vertical Electronic Excitation Energies and Main Excitations Contributing to the Absorption Bands of Zr(^{Me}PDP)$_2$ obtained via TD-DFT Calculations.

Band	TD-DFT State	Energy / cm^{-1} (λ / nm)	f_{osc}	Excitations (weight)[a,b]	Character (%LMCT)
I	1	18,196 (549.6)	0.031	223 → 224 (0.80)	^{1}IL/^{1}LMCT (31%)
	2	18,230 (548.5)	0.032	223 → 225 (0.79)	^{1}IL/^{1}LMCT (31%)
	3	19,975 (500.6)	0.140	222 → 224 (0.71) 222 → 225 (0.15) 223 → 225 (0.10)	^{1}IL/^{1}LMCT (31%)
	4	19,982 (500.4)	0.142	222 → 225 (0.71) 222 → 224 (0.15) 223 → 224 (0.10)	^{1}IL/^{1}LMCT (31%)
II	13	26,739 (374.0)	0.044	219 → 224 (0.83) 219 → 225 (0.11)	^{1}IL/^{1}LMCT (31%)

	14	26,745 (373.9)	0.044	219 → 225 (0.83) 219 → 224 (0.11)	^{1}IL/^{1}LMCT (31%)
	15	27,956 (357.7)	0.136	218 → 225 (0.50) 217 → 224 (0.36)	^{1}IL/^{1}LMCT (31%)
III	21	29,753 (336.1)	0.371	219 → 226 (0.92)	^{1}IL/^{1}LMCT (45%)
IV	30	31,901 (313.5)	0.081	222 → 229 (0.44) 223 → 230 (0.20) 221 → 227 (0.16)	^{1}IL/^{1}LMCT (41%)
	31	31,981 (312.7)	0.082	222 → 230 (0.41) 223 → 229 (0.18) 220 → 227 (0.18)	^{1}IL/^{1}LMCT (41%)
	32	32,322 (309.4)	0.522	222 → 229 (0.38) 221 → 227 (0.20) 218 → 226 (0.16)	^{1}IL/^{1}LMCT (41%)
	33	32,325 (309.4)	0.517	222 → 230 (0.37) 220 → 227 (0.20) 217 → 226 (0.16)	^{1}IL/^{1}LMCT (41%)

[a]only excitations with a weight larger than 0.1 are shown. [b]HOMO 223, LUMO 224, 225 (degenerate).

A qualitative MO diagram for the S_0 state is shown in Figure 4 and allows to characterize the transitions according to the metal and ligand contributions of the donor and acceptor orbitals for each excitation. Notably, the doubly-occupied molecular orbitals 223-217 (HOMO – HOMO-4) that act as donor orbitals in the main TD-DFT excitations observed between 285-1000 nm are exclusively ligand centered. In contrast, the unoccupied molecular orbitals 224-230 (LUMO – LUMO+4) that act as acceptor orbitals in the major TD-DFT excitations in the same wavelength range exhibit significant Zr character with the exception of orbital 227 (LUMO+2). The lowest energy absorption band (I) observed in the electronic absorption spectrum of Zr(^{Me}PDP)$_2$ is comprised of four TD-DFT states that can formally be described as the result of electronic transitions from HOMO and HOMO-1 (orbitals 223 and 222, respectively) to a set of degenerate LUMOs (orbitals 224 and 225). Due to the D_{2d} symmetry of the molecule the four transitions can be grouped into two pairs of degenerate excitations with energies of approximately 18,200 cm^{-1} (549 nm) and 19,980 cm^{-1} (500 nm). Minor deviations from perfect degeneracy are due to the

absence of D_{2d} symmetry constraints during geometry optimization. Because the metal character of the LUMOs was calculated to be 31%, these transitions can be classified as mixed ^{1}IL/^{1}LMCT transitions. While absorption band I (λ_{max}(exp) = 528 nm, λ_{max}(calc) = 500 nm) is the most relevant feature for photocatalysis using visible light excitation, similar assignments were performed to elucidate the nature of the remaining absorption bands II-IV in the higher energy region of the spectrum. Careful analyses of the molecular orbitals involved in the major excitations for these spectral features showed mixed ^{1}IL/^{1}LMCT character for all major excitations observed in the calculated spectrum between 300-400 nm. The amount of ^{1}LMCT contribution for these TD-DFT states is summarized in Table 2.

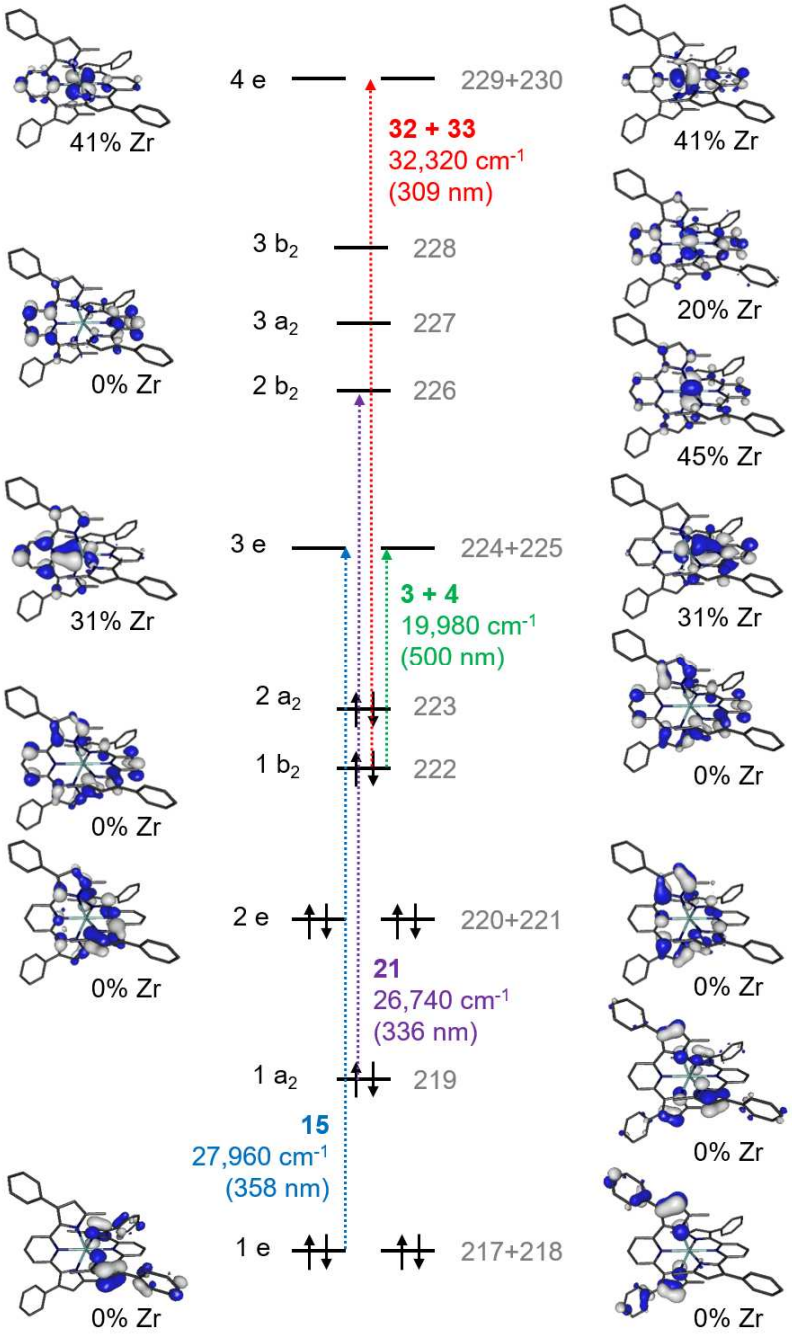

Figure 4. Qualitative MO diagram for Zr(^{Me}PDP)$_2$ showing the donor and acceptor orbitals for TD-DFT excitations computed between 285-1000 nm. Symmetry labels shown to the left of each energy level were assigned according to the D_{2d} point group of the core structure. The gray numbers to the right correspond to the MO number with 223 being the HOMO and 224 and 225 forming a degenerate set of LUMOs. The dotted arrows represent the single electron excitations with the highest weight for the main TD-DFT states of the absorption bands I-IV shown in Figure 3 and Table 2.

Because the long emission lifetime and quenching by triplet oxygen indicated phosphorescent emission from a triplet excited state, the energies of low lying triplet states were investigated computationally. Consistent with the long luminescence lifetime, the lowest excited state of the complex in the S_0 geometry is a triplet state composed of two degenerate TD-DFT excitations with a predicted energy of 16,080 cm^{-1} (621 nm). This value is in agreement with the experimental emission maximum at 595 nm. Three additional triplet excited states were predicted within the energy range of the photocatalytically relevant absorption band I. A Jablonski diagram of the main transitions at calculated wavelengths above 500 nm is shown in Figure 5.

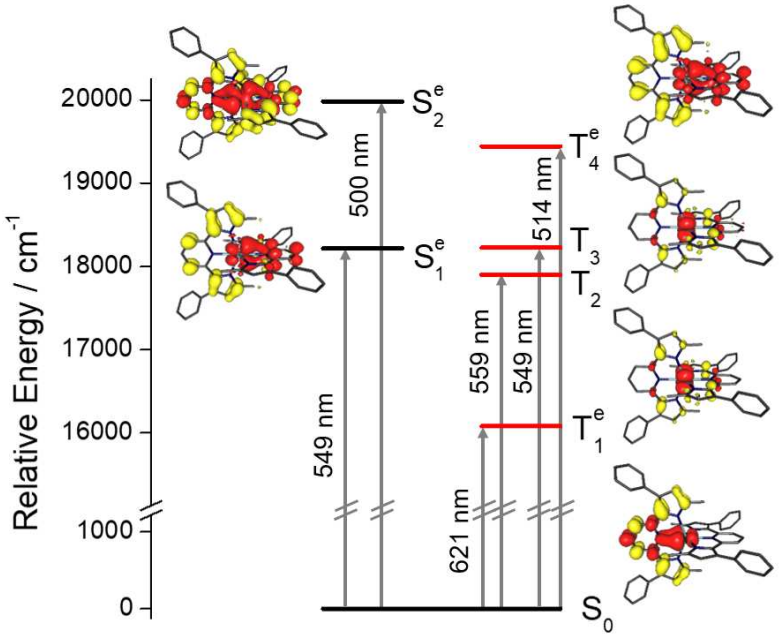

Figure 5. Jablonski diagram of vertical electronic excitations (Franck-Condon states) of $Zr(^{Me}PDP)_2$ in the visible region obtained via TD-DFT calculations. The isosurface plots represent difference density maps for each transition (red: increase in electron density, yellow: decrease in electron density). The superscript e indicates a degenerate state. The second difference density for these states can be obtained via a C_2' operation under D_{2d} symmetry.

The structure of the lowest energy triplet state, T_1, was optimized starting from the S_0 geometry using spin-unrestricted DFT methods (UKS3, S = 1). Important bond distances of the

T_1 geometry are shown in Table 3 alongside the parameters for S_0. Despite the D_{2d} symmetric starting geometry, the triplet state optimization converges to a lower symmetry structure belonging to the C_{2v} point group. Most significantly, the Zr-$N_{pyridine}$ bond distance of one of the ^{Me}PDP units is contracted by more than 0.08 Å compared to the second ligand resulting in an axial compression along the C_2 axis of the molecule. This lowering of the molecular symmetry can be understood as a Jahn-Teller distortion. In a simple one-electron picture, excitation of an electron from the HOMO or HOMO-1 to one of the degenerate LUMOs (corresponding to S_1 and S_2) followed by intersystem crossing results in a T_1 state with a degenerate electron configuration that undergoes an axial compression lowering the overall energy of the system and reducing the symmetry of the molecule. At the same time, the axial distortion results in an electronic structure in which the spin density is localized on zirconium and one of the ^{Me}PDP ligands (Figure 6). The spin density of 0.32 on the zirconium center for T_1 is consistent with a mixed ^{3}IL/^{3}LMCT state and mirrors the 31% ^{1}LMCT character computed for the S_0 and S_1 states.

Table 3. Selected Bond Distances for the S_0 and T_1 Geometries of Zr(^{Me}PDP)$_2$ obtained via DFT Calculations.

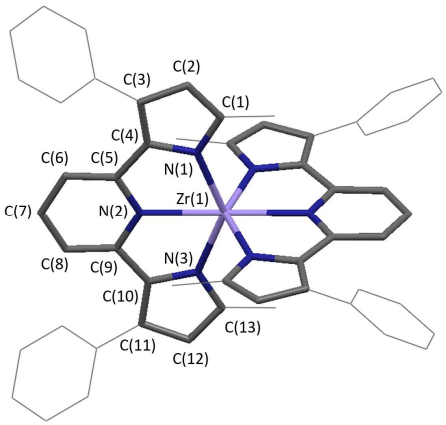

	Singlet (RKS)[a]		Triplet (UKS3)[a]	
	Ligand 1	Ligand 2	Ligand 1	Ligand 2
Zr(1)-N(1)	2.195	2.195	2.221	2.234
Zr(1)-N(2)	2.335	2.335	2.320	2.237
Zr(1)-N(3)	2.194	2.194	2.225	2.237

N(1)-C(1)	1.375	1.375	1.371	1.367
C(1)-C(2)	1.390	1.390	1.392	1.404
C(2)-C(3)	1.423	1.423	1.422	1.408
C(3)-C(4)	1.406	1.406	1.409	1.430
N(1)-C(4)	1.393	1.394	1.396	1.388
C(4)-C(5)	1.445	1.445	1.449	1.432
N(2)-C(5)	1.365	1.365	1.366	1.385
C(5)-C(6)	1.405	1.405	1.405	1.404
C(6)-C(7)	1.394	1.394	1.394	1.405
C(7)-C(8)	1.394	1.394	1.394	1.395
C(8)-C(9)	1.405	1.405	1.405	1.408
N(2)-C(9)	1.365	1.365	1.366	1.394
C(9)-C(10)	1.445	1.445	1.448	1.422
N(3)-C(10)	1.394	1.393	1.396	1.383
C(10)-C(11)	1.406	1.406	1.410	1.448
C(11)-C(12)	1.423	1.423	1.421	1.399
C(12)-C(13)	1.390	1.390	1.392	1.410
N(3)-C(13)	1.375	1.376	1.370	1.373

[a]No symmetry constraints were applied during geometry optimization.

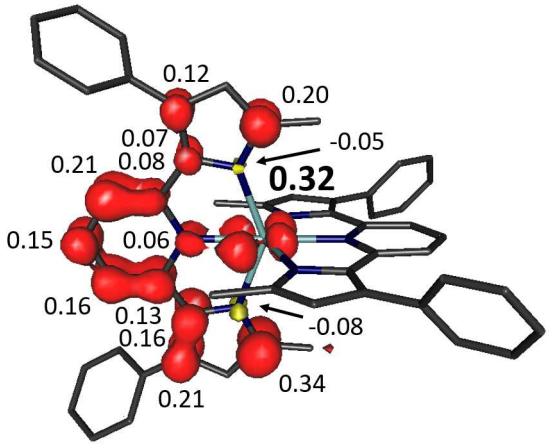

Figure 6. Spin density distribution for the lowest energy triplet state of $Zr(^{Me}PDP)_2$ obtained via Mulliken population analysis.

Based on our (TD-)DFT studies, we propose the following hypothesis for the generation of a long-lived triplet excited state in $Zr(^{Me}PDP)_2$ during photoredox catalytic turnover. Photoexcitation of the S_0 state with visible light (green LED, λ_{max} = 521 nm, FWHM = 36 nm) generates $^1IL/^1LMCT$ excited states, S_1 and S_2, with 31% ^1LMCT character. Under Franck-Condon conditions the initial excited state retains D_{2d} symmetry and the change in charge distribution is delocalized over both ^{Me}PDP ligands via the zirconium d_{xz} and d_{yz} orbitals. The degenerate nature of the S_1 and S_2 states allows for strong spin-orbit coupling mediated by the Zr d_{xz} and d_{yz} contributions to the degenerate LUMOs and facilitates rapid intersystem crossing to the triplet manifold. Vibrational cooling results in a localized T_1 state with reduced C_{2v} symmetry. The lowered symmetry lifts the degeneracy of the d_{xz} and d_{yz} orbitals and reduces spin-orbit coupling resulting in the remarkably long lifetime observed experimentally.

Stern-Volmer Quenching Experiments. Having established the emission lifetime and a computational model for the electronic structure of the excited state, we extended our previous Stern-Volmer quenching studies to obtain further insight into the mechanistic steps following photon absorption during bibenzyl formation. A comparison of the Stern-Volmer plots for the three previously reported ^{R}BIH derivatives and the new sacrificial reductant ^{MeO}BIH are shown in Figure 7. The strictly linear dependence of the luminescence intensities on the concentration of the quencher is indicative of diffusion-controlled dynamic quenching processes without pre-association of $Zr(^{Me}PDP)_2$ and ^{R}BIH. The obtained Stern-Volmer constants, K_{SV}, and the corresponding quenching rate constants, k_q, are summarized in Table 4. The inclusion of ^{MeO}BIH further establishes the strong correlation between oxidation potential of the ^{R}BIH derivative and the quenching rate supporting a photo-induced SET step. Individual quenching experiments for

the remaining components of the reaction mixture established that neither benzyl bromide nor NEt_3 are suitable quenchers for the excited state of $Zr(^{Me}PDP)_2$. The absence of quenching by NEt_3 is an important distinction from classic precious metal photoredox catalysts such as $[Ru(bpy)_3]^{2+}$ and $Ir(ppy)_3$ and highlights the substantially more negative ground and excited state redox potentials of $Zr(^{Me}PDP)_2$, which necessitate more powerful sacrificial reductants. The absence of quenching by benzyl bromide rules out a potential oxidative quenching pathway. As a whole, the Stern-Volmer experiments strongly support reductive quenching by ^{R}BIH as the first step following photoexcitation.

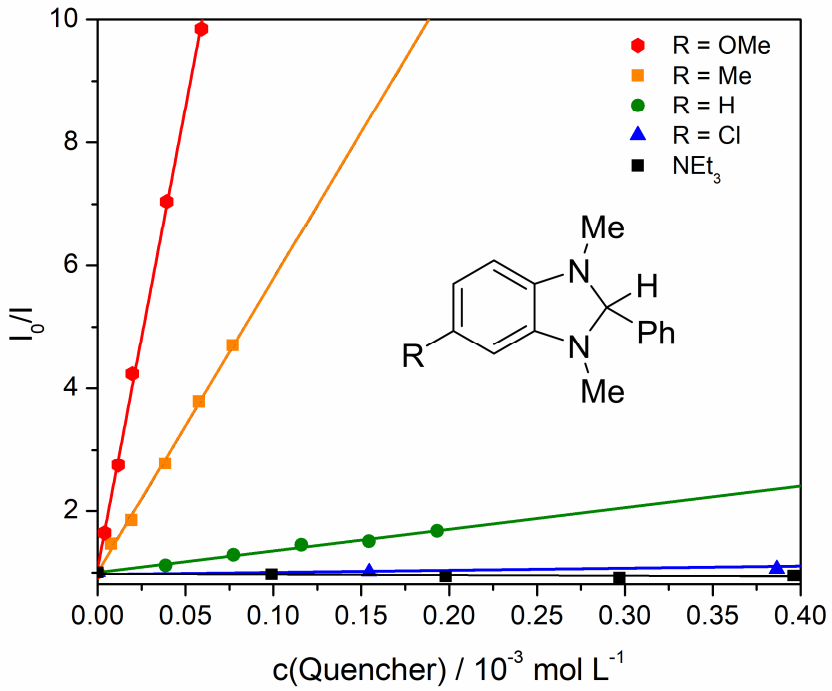

Figure 7. Stern-Volmer plots obtained via steady-state emission spectroscopy.

Table 4. Quenching parameters from Stern-Volmer analysis and redox potentials.

	K_{SV} / L mol^{-1}	k_q / 10^7 L mol^{-1} s^{-1}	E_{ox} / V vs. $Fc^{+/0}$
^{MeO}BIH	150,000 ± 2000	46.15	-0.25[b]

^{Me}BIH	47,900 ± 600[a]	14.74	-0.16[b]
^{H}BIH	3,500 ± 100[a]	1.08	-0.10[b]
^{Cl}BIH	340 ± 50	0.10	0.00[b]
NEt_3	no quenching		0.47[c]
BnBr	no quenching		n.a.

[a] from reference 78. [b] from reference 79. [c] from reference 87.

Synthesis, Characterization, and Reactivity of the Reduced Photosensitizer. The reductive quenching pathway indicated by the Stern-Volmer quenching studies prompted attempts to isolate the one-electron reduced form of the photosensitizer. The cyclic voltammogram (Figure S8) guided the choice of a sufficiently strong single electron reductant for the first reversible reduction event in Zr(^{Me}PDP)$_2$ at -2.16 V vs. Fc^+/Fc.[78]

Scheme 1. Synthesis of $[Zr(^{Me}PDP)_2]^{1-}$ via alkali metal reduction of Zr(^{Me}PDP)$_2$.

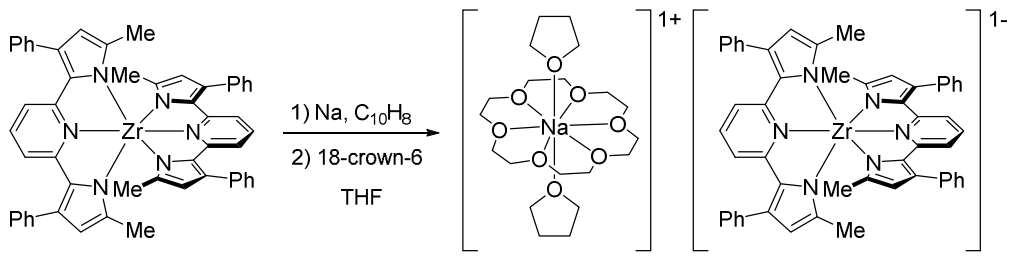

Addition of one equivalent of a freshly prepared sodium naphthalenide in THF solution to Zr(^{Me}PDP)$_2$ in the presence of 1,4,7,10,13,16-hexaoxacyclooctadecane, 18-crown-6, resulted in an immediate color change from pink to dark purple. Removal of solvent and recrystallization from THF/toluene at -35 °C yielded a dark purple crystalline solid identified as [Na(18-crown-6)(thf)$_2$][Zr(^{Me}PDP)$_2$] in 84% yield (Scheme 1). The ^{1}H NMR spectrum recorded in THF-d_8 exhibits several paramagnetically broadened signals consistent with the formation of D_{2d} symmetric $[Zr(^{Me}PDP)_2]^{1-}$ in solution. A comparison of the electronic absorption spectra of

[Na(18-crown-6)(thf)$_2$][Zr(^{Me}PDP)$_2$] in THF and the starting material Zr(^{Me}PDP)$_2$ is shown Figure 8. The most notable difference is the appearance of a broad absorption band with a maximum at 649 nm (ε = 2,200 M^{-1} cm^{-1}). Two additional features are observed as a band with a maximum at 516 nm (ε = 19,070 M^{-1} cm^{-1}) and a shoulder around 550 nm. These two features appear at similar wavelengths as the main visible absorption band in Zr(^{Me}PDP)$_2$ albeit with slightly reduced intensity.

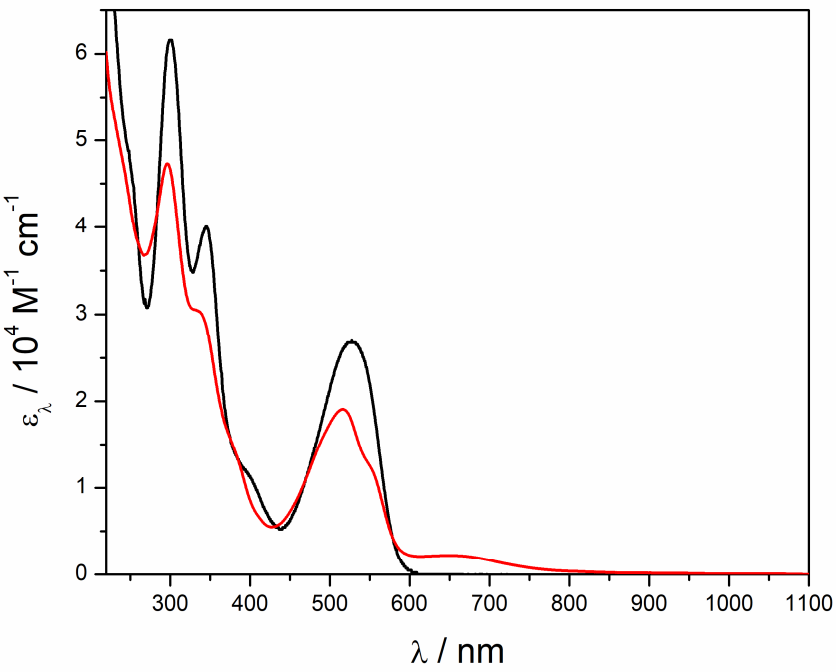

Figure 8. Comparison of the electronic absorption spectra of [Na(18-crown-6)(thf)$_2$][Zr(^{Me}PDP)$_2$] and Zr(^{Me}PDP)$_2$ in THF at room temperature.

The solid state structure of [Na(18-crown-6)(thf)$_2$][Zr(^{Me}PDP)$_2$] was determined by X-ray diffraction and representations of the molecular structures of the cationic and anionic portions are shown in Figure 9. Comparison of the structural parameters with those obtained previously for the neutral form of the photosensitizer allowed further evaluation of the effects of one-electron reduction on the geometry of the complex and provided insight into the electronic

structure of $[Zr(^{Me}PDP)_2]^{1-}$ (Table 5). We have recently shown that the PDP scaffold can act as a redox-active ligand under highly reducing conditions, which raised the question whether reduction in the $Zr(^{Me}PDP)_2/[Zr(^{Me}PDP)_2]^{1-}$ redox couple is metal- or ligand-centered. The overall changes to the molecular structure upon reduction of $Zr(^{Me}PDP)_2$ are remarkably small. For the metal-ligand bond distances a slight decrease by 0.039 Å is observed in the average Zr-N_{py} bond length while an even smaller increase by 0.030 Å can be noted for the average Zr-$N_{pyrrole}$ bond length. The changes in the intra-ligand bond distances are even subtler. Previous studies on the related group VI complexs $[M(^{Me}PDP)_2]^z$ (M = Cr, Mo; z = 1-, 2-) established that changes in the pyridine C-N_{py} bond lengths are the most reliable reporter of the redox state of the PDP ligand.[88] While the dianionic form of the ligand typically exhibits C-N_{py} bond lengths of 1.355 – 1.365 Å, as observed for the neutral complex $Zr^{IV}(^{Me}PDP^{2-})_2$ (average C-N_{py} = 1.361 Å), formation of a metal-bound radical trianion, $^{Me}PDP^{\bullet 3-}$, is associated with C-N_{py} bond elongation to 1.390 – 1.410 Å. The average C-N_{py} bond lengths of 1.380 Å in $[Zr(^{Me}PDP)_2]^{1-}$ falls in-between these two ranges, while changes in the remaining intra-ligand bond distances are < 0.02 Å and cannot be considered significant within the resolution of the experiment. The experimental data are consistent with two electronic structure descriptions: a) ligand-centered reduction, in which the radical is delocalized over both ligands or b) strong metal-ligand covalency, where the unpaired electron occupies an orbital with significant contributions from both Zr and the ^{Me}PDP ligand. This ambiguity emphasizes the difficulty in unequivocally establishing an electronic structure based on geometric parameters alone and prompted further spectroscopic and computational studies.

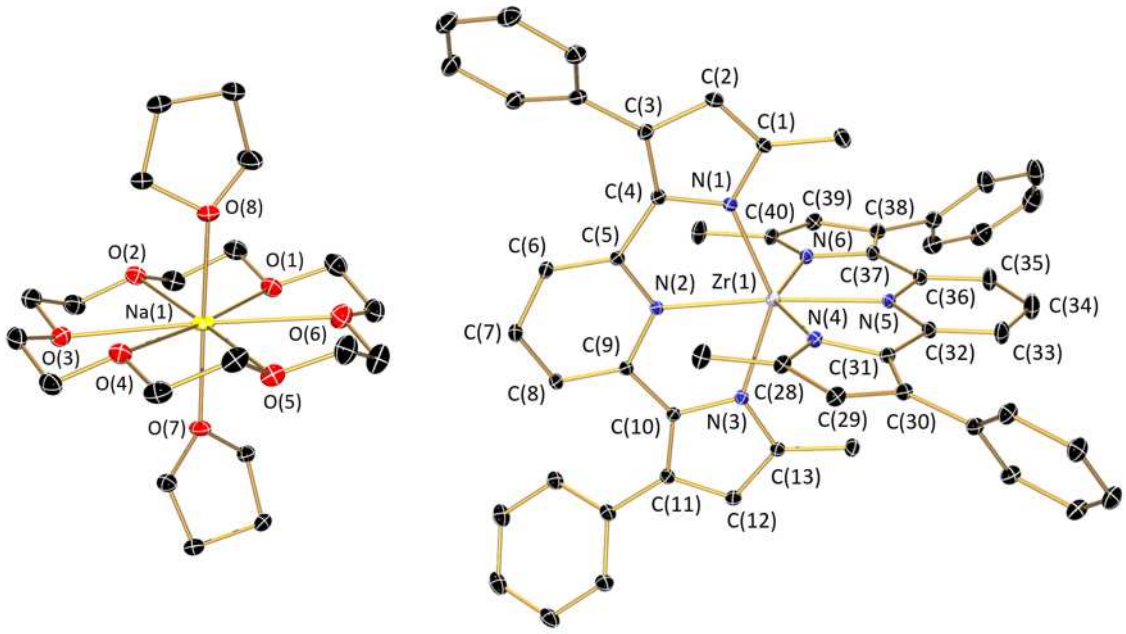

Figure 9. Representation of the molecular structures of $[Na(18\text{-crown-}6)(thf)_2]^{1+}$ (left) and $[Zr(^{Me}PDP)_2]^{1-}$ (right) at 30% probability ellipsoids. Hydrogen atoms were omitted for clarity.

Table 5. Selected Bond Lengths (Å) and Angles (°) for $[Zr(^{Me}PDP)_2]^z$ (z = 0, 1-).

	$Zr(^{Me}PDP)_2$ [a]	$[Zr(^{Me}PDP)_2]^{1-}$ [b]
Zr(1)-N(1)	2.151(3)	2.181(2)
Zr(1)-N(2)	2.288(3)	2.266(2)
Zr(1)-N(3)	2.183(3)	2.192(2)
Zr(1)-N(4)	2.143(3)	2.199(2)
Zr(1)-N(5)	2.300(3)	2.243(2)
Zr(1)-N(6)	2.171(3)	2.197(2)
N(2)-C(5)	1.364(5)	1.375(2)
C(5)-C(6)	1.387(5)	1.391(3)
C(6)-C(7)	1.376(6)	1.394(3)
C(7)-C(8)	1.383(6)	1.393(3)
C(8)-C(9)	1.383(5)	1.392(3)
N(2)-C(9)	1.362(5)	1.382(2)
N(5)-C(32)	1.361(5)	1.389(2)
C(32)-C(33)	1.384(5)	1.384(3)
C(33)-C(34)	1.381(5)	1.389(3)
C(34)-C(35)	1.385(5)	1.405(3)
C(35)-C(36)	1.387(5)	1.379(3)
N(5)-C(36)	1.358(5)	1.372(2)

Dihedral	88.30	88.81
N(2)-Zr(1)-N(5)	171.76(8)	174.84(6)

[a]from reference [78]. [b]from $[Na(18\text{-crown-6})(thf)_2][Zr(^{Me}PDP)_2]\cdot 3THF$.

The X-band EPR spectrum of $[Na(18\text{-crown-6})(thf)_2][Zr(^{Me}PDP)_2]$ recorded in frozen THF/toluene solution at 80 K is shown in Figure 10. The observed axial signal clearly establishes the S = 1/2 ground state of $[Zr(^{Me}PDP)_2]^{1-}$. The data were simulated using a spin Hamiltonian with g values of $g_{\perp} = 1.998$ and $g_{\parallel} = 1.971$. Coupling to ^{91}Zr ($I = 5/2$, natural abundance = 11.22%) was taken into account by a hyperfine coupling constant of $A_{\perp}(^{91}Zr) = 30$ MHz and nicely reproduces the additional feature in the low field region of the spectrum. No hyperfine splitting was resolved in the high field region of the spectrum. The magnitude of the ^{91}Zr hyperfine coupling and the significant deviation from the g value of the free electron ($g_e = 2.0023$) towards lower g values are consistent with significant Zr contributions to the SOMO of $[Zr(^{Me}PDP)_2]^{1-}$.

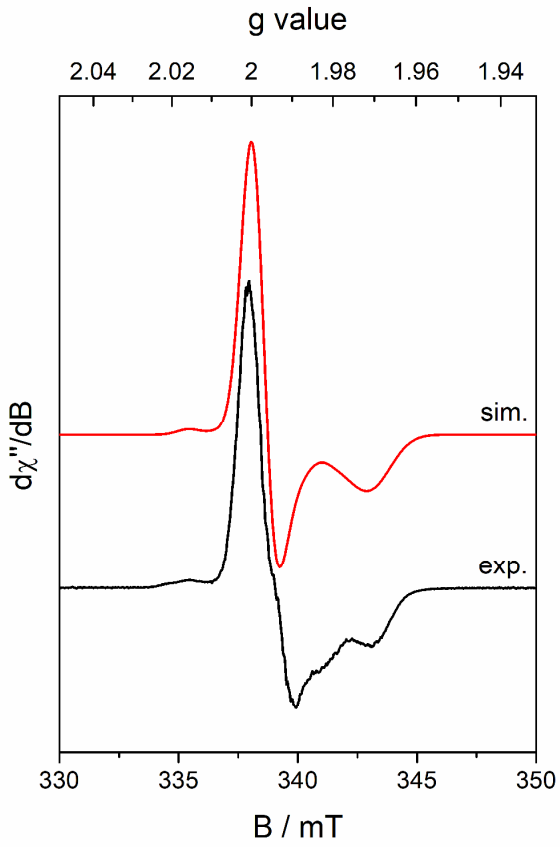

Figure 10. X-band EPR spectrum of $[Zr(^{Me}PDP)_2]^{1-}$ in frozen THF/toluene solution recorded at 80 K (experimental parameters: frequency = 9.463 GHz, power = 0.4 mW, modulation: 2 G). See text for simulation parameters.

To support the spectroscopic studies, full molecule density functional theoretical (DFT) calculations were conducted at the B3LYP level. The geometric parameters from geometry optimization are in excellent agreement with the experimental structure from X-ray crystallography. The spin density distribution obtained via Mulliken population analysis is shown in Figure 11 and reveals the highly delocalized nature of the SOMO in $[Zr(^{Me}PDP)_2]^{1-}$ with near equal contributions of 48% from the metal center and 52% from the two ^{Me}PDP ligands consistent with the structural data. Further inspection of the molecular orbital manifold shows that the metal character in the SOMO results from close to equal contributions of the d_{xz} and d_{yz} orbitals that form a degenerate e set under the idealized D_{2d} symmetric ligand field. This result is surprising given that the T_1 state calculated for neutral $Zr(^{Me}PDP)_2$, which can also be described

as containing a single electron in the e set, undergoes a Jahn-Teller distortion resulting in a symmetry lowering to C_{2v}. While this effect might be weaker for the doublet ground state of $[Zr(^{Me}PDP)_2]^{1-}$ compared to a triplet system, calculations using the conductor-like screening model (COSMO) were conducted to simulate the effects of a dielectric medium. This approach has previously been shown to favor localized electronic structures in systems containing redox-active ligands.[89] Consistent with these previous studies, the optimized geometry using COSMO exhibits C_{2v} symmetry most clearly established by the two different Zr-$N_{pyridine}$ bond distances (2.333 Å and 2.235 Å) for the two ligands. This structure is the result of delocalization of the unpaired electron between the Zr center (42%) and only one of the two ^{Me}PDP ligands (58%) and removes the degeneracy of the d_{xz} and d_{yz} orbitals. It should be noted however, that the electronic structures with D_{2d} and C_{2v} symmetry are likely to interconvert via vibronic coupling under experimental conditions.

Both electronic structures with degenerate or near-degenerate d_{xz} and d_{yz} orbitals are consistent with the observed axial EPR spectrum. Strong spin-orbit coupling in the d_{xz}, d_{yz} manifold results in significant orbital angular momentum contributions and deviation of the $g_{\parallel}$ value from 2.0023. In contrast, spin-orbit coupling involving the d_{xy} orbital that result in deviations for $g_{\perp}$ are reduced due to the strong destabilization of this orbital by the four pyrrolate π donors. Reassuringly, DFT (CP-SCF) calculations of the g values for $[Zr(^{Me}PDP)_2]^{1-}$ ($g_{\perp}$ = 2.000, $g_{\parallel}$ = 1.957) are in excellent agreement with the experimental parameters. Based on the combined experimental and computational results the electronic structure of the reduced from of the photosensitizer, $[Zr(^{Me}PDP)_2]^{1-}$, is best described as a hybrid of the limiting resonance structures $[Zr^{III}(^{Me}PDP^{2-})_2]^{1-}$ and $[Zr^{IV}(^{Me}PDP^{\bullet 3-})(^{Me}PDP^{2-})]^{1-}$.

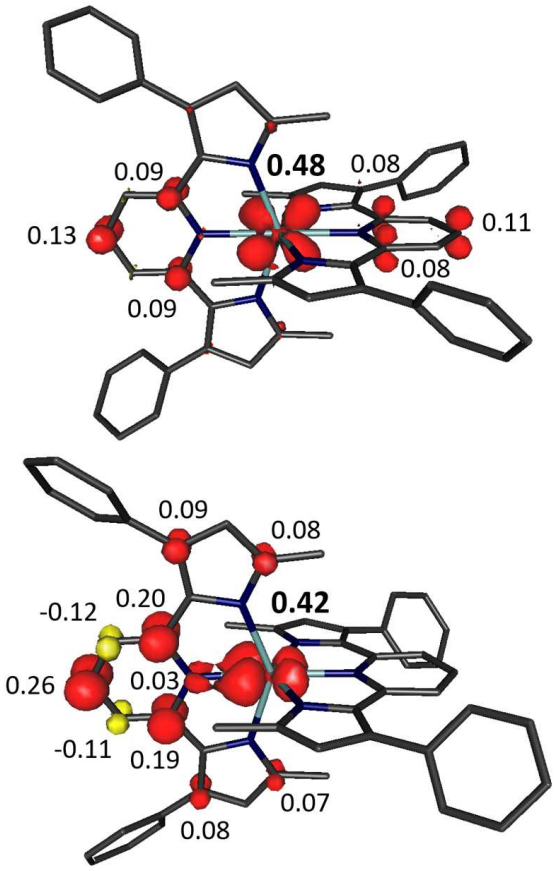

Figure 11. Spin density distribution obtained via Mulliken population analysis for $[Zr(^{Me}PDP)_2]^{1-}$ with (bottom) and without (top) using the COSMO approximation.

With the isolated complex $[Na(18\text{-crown-6})(thf)_2][Zr(^{Me}PDP)_2]$ in hand, the reactivity of the reduced photosensitizer towards benzyl bromide was explored to establish whether $[Zr(^{Me}PDP)_2]^{1-}$ can act as the active single-electron reductant in the photocatalytic homocoupling reaction. Slow addition of a dilute solution of $[Na(18\text{-crown-6})(thf)_2][Zr(^{Me}PDP)_2]$ in THF to a solution containing 10 equivalents of benzyl bromide at room temperature resulted in an immediate reaction yielding bibenzyl and $Zr(^{Me}PDP)_2$ as the major products identified by ^1H NMR spectroscopy (Scheme 2). Slow addition and low concentrations of $[Zr(^{Me}PDP)_2]^{1-}$, simulating the slow but continuous generation of this species under photoredox catalytic conditions, proved to be critical. High concentrations of the reduced zirconium species resulted

in poor yield of bibenzyl and formation of a new diamagnetic zirconium species in addition to $Zr(^{Me}PDP)_2$. While this new complex has so far eluded isolation and further characterization, preliminary ^1H NMR data indicate a compound with a modified ^{Me}PDP ligand likely due to reaction of benzyl radical with a second equivalent of $[Zr(^{Me}PDP)_2]^{1-}$. These reactivity studies clearly show that $[Zr(^{Me}PDP)_2]^{1-}$ is a potent one-electron reductant that can facilitate the formation of bibenzyl from benzyl bromide.

Scheme 2. Reactivity of $[Na(18\text{-crown-}6)(thf)_2][Zr(^{Me}PDP)_2]$ with benzyl bromide.

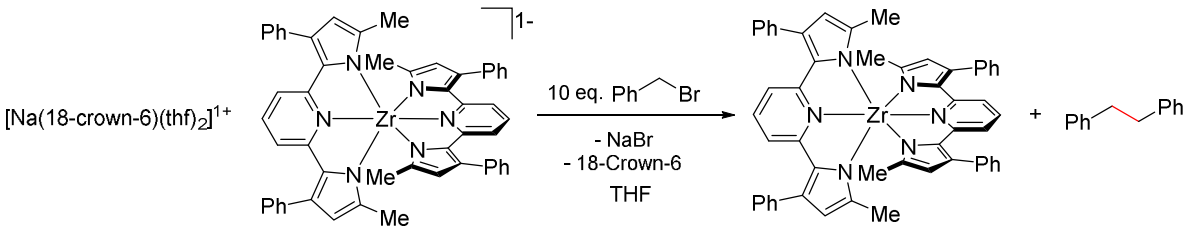

Synthesis, Characterization, and Reactivity of $(^{R}BI)_2$ Derivatives. The versatile PCET pathways reported for a wide variety of benzimidazolium hydrides[79] motivated further studies of the fate of the sacrificial reductant after photo-induced single-electron transfer (SET). The critical role of the base observed in the optimization of the catalytic conditions indicated that benzimidazolyl radicals, $^{R}BI^{\bullet}$, formed via deprotonation of the oxidized reductant, $^{R}BIH^{\bullet+}$, could play a key-role during catalytic turnover. Electrochemical studies of 2-aryl-benzimidazolium halide salts suggest that the one-electron reduced species could serve as potent single-electron reductants with redox potentials ranging from -1.80 V to -2.10 V vs. Fc^+/Fc depending on the substitution patterns.[79] While synthetic routes to 2-alkyl substituted benzimidazolyl radicals via reduction of benzimidazolium halide salts have been reported,[90,91] isolation and characterization of 2-aryl substituted derivatives proposed and targeted in this study have remained elusive.

Addition of one equivalent of freshly prepared sodium naphthalenide solution to a suspension of 1,3-dimethyl-2-phenyl-1H-benzimidazolium iodide, (^{H}BI)I, in THF resulted in the immediate formation of a clear, yellow solution. Recrystallization of the crude reaction product from toluene and pentane at -35 °C yielded colorless crystals of (^{H}BI)$_2$, the dimerization product of the targeted radical ^{H}BI$^{\bullet}$ (Scheme 3). The methoxy-substituted derivative (^{MeO}BI)$_2$ was prepared via the same protocol.

Scheme 3. Synthesis of (^{H}BI)$_2$ via alkali metal reduction of (^{H}BI)I.

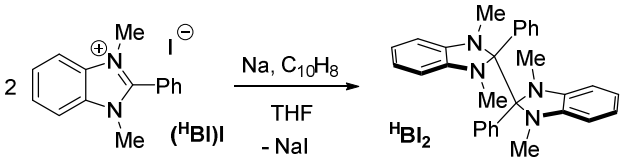

The identity of (^{H}BI)$_2$ was established by NMR spectroscopy and X-ray crystallography and a representation of the molecular structure in the solid state is shown in Figure 12. A remarkable feature of this extremely air- and moisture-sensitive compound is the long C(1)-C(1)' bond distance of 1.579(4) Å between the two halves of the dimer. In combination with significantly broadened resonances observed in the ^{1}H NMR spectrum of (^{H}BI)$_2$ this weakened C-C bond raised questions about a potential equilibrium between the dimeric species and the monomeric radical in solution. Similar equilibria have been established for the corresponding 2-alkyl derivatives via variable temperature EPR studies.[90] In contrast to these alkyl-substituted species, however, we found no evidence for free radical formation was obtained for (^{H}BI)$_2$ or (^{MeO}BI)$_2$ in solution at room temperature via EPR spectroscopy. Consistent with this observation, variable-temperature NMR studies revealed a sharpening of resonances at elevated temperatures,

suggesting that the broadening can be attributed to restricted rotation about the C(1)-C(1)' bond rather than a dimer/monomer equilibrium.

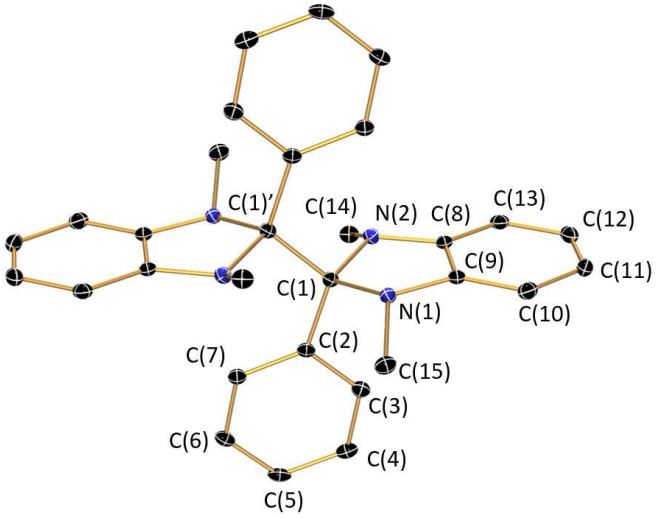

Figure 12. Representation of the solid state molecular structure of $(^{H}BI)_2$ at 30% probability ellipsoids. Hydrogen atoms were omitted for clarity.

Despite the lack of detectable amounts of free radical in solution, the reactivity of the two isolable $(^{R}BI)_2$ derivatives (R = H or OMe) was investigated. Addition of $(^{R}BI)_2$ to a THF solution containing ten equivalents of benzyl bromide resulted in the rapid formation of $(^{R}BI)Br$ and bibenzyl in approximately 2:1 ratio (Scheme 4). This experiment clearly establishes that $(^{R}BI)_2$ derivatives are competent reductants for the reductive homocoupling of benzyl bromide. In addition to simple redox chemistry, photo-induced electron transfer between $(^{MeO}BI)_2$ and $Zr(^{Me}PDP)_2$ was investigated via Stern-Volmer quenching experiments. Importantly, no ground state electron transfer between the two compounds was detected, which was readily established by comparison of the electronic absorption spectra of the photosensitizer in the presence and absence of $(^{MeO}BI)_2$. The Stern-Volmer analysis clearly demonstrates that $(^{MeO}BI)_2$ acts as a

powerful quencher for the excited state of $Zr(^{Me}PDP)_2$ with a quenching rate constant, k_q, of 1.74 x 10^9 L mol^{-1} s^{-1}.

Scheme 4. Reactivity of $(^{H}BI)_2$ with benzyl bromide.

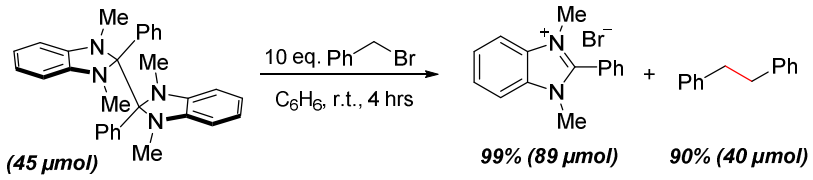

Detection of Radical Intermediates During Photoredox Catalytic Turnover. Two different experiments were conducted to provide evidence for the generation of radical intermediates via photo-induced SET (Scheme 5). In the first experiment, the photocatalytic reaction was performed in the presence of two equivalents of the stable radical 2,2,6,6-tetramethylpiperidin-1-yl)oxyl (TEMPO). Under these conditions, the formation of bibenzyl and toluene was suppressed completely. Instead, a significant amount of 1-benzyloxy-2,2,6,6-tetramethylpiperidine (^{Bn}TEMPO) was detected by ^{1}H NMR[92] and isolated from the reaction mixture via chromatography. The formation of ^{Bn}TEMPO indicates the presence of benzyl radical under catalytic conditions, which is the expected product of the proposed one-electron reduction of benzyl bromide in a photoredox catalytic mechanism.

Scheme 5. Radical trapping experiments using the persistent radical TEMPO and the spin trap DMPO.

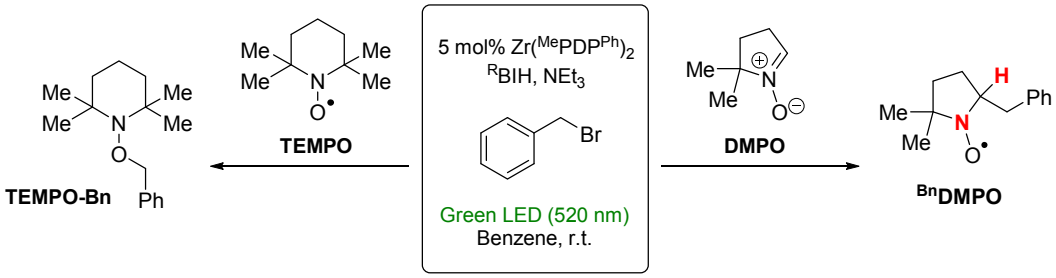

To further corroborate this result, a second radical trapping experiment was performed using 5,5-dimethyl-1-pyrroline-*N*-oxide (DMPO) as a spin trap for the detection of short-lived radical species. An aliquot of the reaction mixture including three equivalents of DMPO was prepared under low light conditions and placed in the cavity of an EPR spectrometer allowing irradiation with green light (LED, λ_{max} = 520 nm) directly in the spectrometer. The EPR spectra of the reaction mixture in the dark and under green light illumination are shown in Figure 13. The signal obtained upon irradiation shows six hyperfine lines of equal intensity and was readily simulated as a doublet of triplets centered at g_{iso} = 2.008 resulting from hyperfine coupling to one proton (^{1}H, I = 1/2, natural abundance = 99.98%) and one nitrogen (^{14}N, I = 1, natural abundance = 99.64%) with coupling constants of $A_{iso}(^{1}H)$ = 58 MHz and $A_{iso}(^{14}N)$ = 39 MHz, respectively. These values are in excellent agreement with the EPR parameters reported for the benzyl radical adduct of DMPO (^{Bn}DMPO)[93] supporting radical formation and a photoredox catalytic mechanism. The signal intensity for the persistent *N*-oxyl radical rapidly reaches a maximum upon irradiation, which is consistent with the fact that ^{Bn}DMPO can react with a second equivalent of benzyl radical to generate a diamagnetic species.

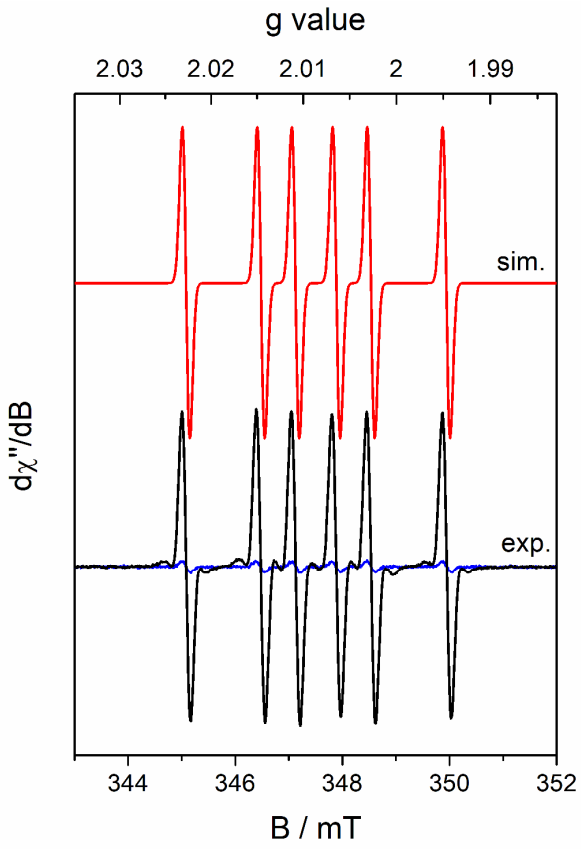

Figure 13. Room temperature X-band EPR spectrum of ^{Bn}DMPO in benzene solution (black); simulated spectrum (red). ^{Bn}DMPO was generated under photocatalytic conditions in the presence of DMPO by irradiation (LED, 520 nm) in the EPR cavity. The blue line represents the spectrum of the reaction mixture before irradiation. The small amount of ^{Bn}DMPO is likely due to ambient light irradiation during sample preparation.

Proposed Photoredox Catalytic Cycle. The combination of the individual experiments presented in this work provides a detailed picture of the mechanism of bibenzyl formation via benzyl bromide homocoupling under photocatalytic conditions (Scheme 6). Visible light absorption by the photosensitizer Zr(^{Me}PDP)$_2$ generates a long-lived excited state, Zr(^{Me}PDP)$_2$*, with significant ^{3}LMCT character. Photo-induced SET between Zr(^{Me}PDP)$_2$* and the sacrificial reductant ^{R}BIH results in reductive quenching of the excited state and yields the highly reducing complex [Zr(^{Me}PDP)$_2$]$^{1-}$. This complex can in turn transfer an electron to benzyl bromide resulting in the formation of a benzyl radical, as detected by radical trapping experiments, and regeneration of the photosensitizer. The oxidized reductant ^{R}BIH$^{\bullet+}$ is readily deprotonated by

NEt_3 to generate the strong reductant $^{R}BI^{\bullet}$, which can either act as a strong reductant and efficient quencher for $Zr(^{Me}PDP)_2$* (A) or undergo direct SET with benzyl bromide yielding benzyl radical (B). A third route resulting in dimerization to $(^{R}BI)_2$ is unlikely under turnover conditions due to the expected low concentration of $^{R}BI^{\bullet}$. Independent of the pathway, ^{R}BIH can act as a two-electron donor resulting in the formation of $^{R}BI^{+}$, which is consistent with the observation that less than one equivalent of ^{R}BIH are required for complete conversion of benzyl bromide. Lastly, radical-radical homocoupling yields the final product bibenzyl. This mechanism is akin to the one proposed and investigated recently for the $[Ir(ppy)_2(dtbbpy)]^{+}$ (ppy = 2-phenylpyridine, dtbbpy = 4,4'-di-tert-butyl-2,2'-bipyridine) catalyzed homocoupling of benzylbromide using Hantzsch ester as the sacrificial reductant.[94]

Scheme 6. Proposed mechanism for the photoredox catalytic coupling of benzyl bromide with $Zr(^{Me}PDP)_2$ as the photosensitizer.

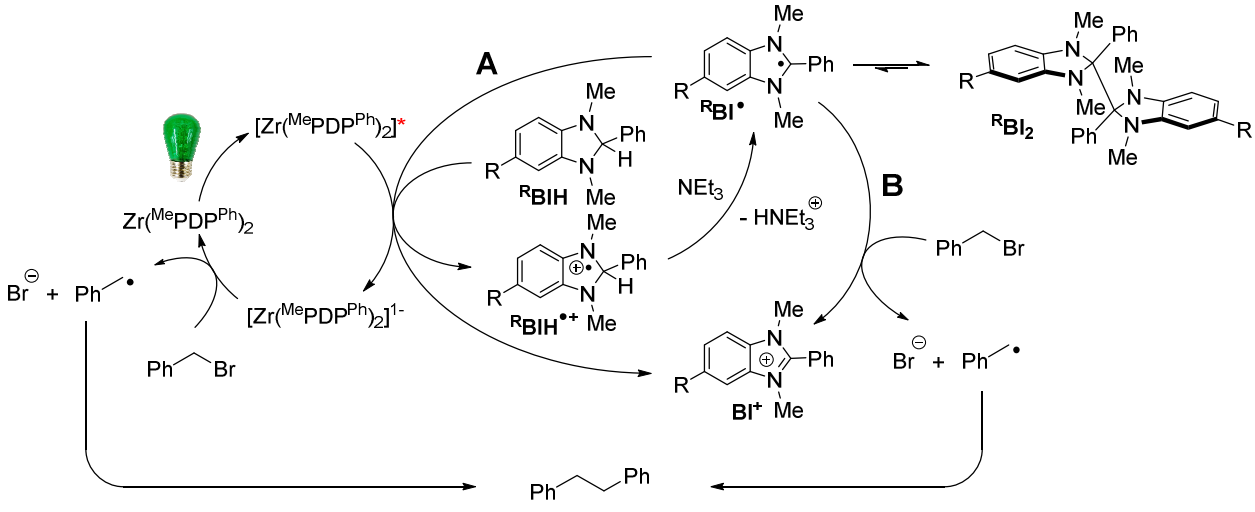

Concluding Remarks

In this study, we have demonstrated that the excited state of the luminescent zirconium complex $Zr(^{Me}PDP)_2$ exhibits a remarkably long lifetime of 325 μs that is consistent with

phosphorescent emission due to a spin-forbidden $T_1 \rightarrow S_0$ transition. This value is among the longest lifetimes reported for transition metal complexes and exceeds the values found in traditional MLCT photosensitizers. Based on our computational analysis of the absorption spectrum of $Zr(^{Me}PDP)_2$ using TD-DFT and elucidation of the electronic structure of the lowest energy triplet state of $Zr(^{Me}PDP)_2$ by DFT, we propose that the emissive state is best described as a mixed ^{3}IL/^{3}LMCT state with 31% LMCT character due to high covalency between zirconium and the pyridine moieties of the ligand. Stern-Volmer quenching studies using benzimidazolium hydrides as sacrificial electron donors suggest that the excited state undergoes facile single-electron transfer to generate $[Zr(^{Me}PDP)_2]^{1-}$ under photocatalytic conditions. Independent isolation of this highly reducing species allowed us to establish its electronic structure via structural and spectroscopic studies supported by DFT calculations. Our results indicate that the complex is best described as a hybrid of the limiting resonance structures $[Zr^{III}(^{Me}PDP^{2-})_2]^{1-}$ and $[Zr^{IV}(^{Me}PDP^{\bullet 3-})(^{Me}PDP^{2-})]^{1-}$. Based on this electronic structure description, the Zr center plays a significant role in the SET chemistry of $Zr(^{Me}PDP)_2$ and is not simply a redox-innocent scaffold holding the two organic ligands in place.

To further establish the capacity of $Zr(^{Me}PDP)_2$ to facilitate photoredox processes via photo-induced single-electron transfer, the role of the proposed intermediates $[Zr(^{Me}PDP)_2]^{1-}$ and $^{R}BI^{\bullet}$ was evaluated using the homocoupling of benzyl bromide to bibenzyl as a model reaction. In combination with radical trapping experiments under photocatalytic turnover, these mechanistic studies are consistent with a photoredox catalytic mechanism using $Zr(^{Me}PDP)_2$ as a photosensitizer.

Experimental Section

Preparation of [Na(18-crown-6)(thf)$_2$][Zr(^{Me}PDP)$_2$]. In the drybox, a 20 mL scintillation vial was charged with a solution of Zr(^{Me}PDP)$_2$ (55 mg, 0.064 mmol) and 18-crown-6 (17 mg, 0.064 mmol, 1.01 equiv) in 2 mL of THF. A freshly prepared solution of sodium naphthalenide (11 mg naphthalene, 0.070 mmol, 1.10 equiv) in THF (3 mL) was added slowly upon which the color of the reaction mixture changed to dark purple within seconds. The reaction was allowed to stir at room temperature for 3 hours. THF was removed in vacuum and the last traces of the solvent were removed by co-evaporation with Et_2O. The resulting solid residue was washed five times with pentane to remove naphthalene. The crude product was redissolved in THF, filtered, and recrystallized from THF and toluene cooled to -35 °C. The product was collected by filtration as dark purple crystals (Yield: 70 mg, 84%). X-ray quality single crystals of [Na(18-crown-6)(thf)$_2$][Zr(^{Me}PDP)$_2$]·3THF were grown from THF and Et_2O solution at −35 °C. ^{1}H NMR (400 MHz, THF-d_8; δ, ppm): 22.40 (br), 11.96 (br), 3.58 (s, THF), 3.42 (br, 18-crown-6), 1.73(s, THF), -2.54 (br), -3.19 (br). Three additional signals expected for D_{2d} symmetric [Zr(^{Me}PDP)$_2$]$^{1-}$ could not be detected, which is likely due to paramagnetic broadening. Anal. Calcd for $C_{74}H_{82}N_6NaO_8Zr$: C, 68.49; H, 6.37; N, 6.48; Found: C, 65.23; H, 5.83; N, 6.47. Multiple attempts to obtain more satisfactory elemental analysis were unsuccessful due to the high sensitivity of the compound.

Preparation of *N,N*'-dimethyl-2-phenyl-benzo[d]imidazoline dimer (^{H}BI)$_2$. In the drybox, a 50 mL round-bottom flask was charged with (^{H}BI)I (160 mg, 0.457 mmol). THF (10 mL) was added and the resulting suspension was stirred for 30 minutes. A freshly prepared solution of sodium naphthalenide (76 mg naphthalene, 0.502 mmol, 1.10 equiv) in THF was added dropwise to the reaction mixture. A clear yellow solution was obtained after completion of the sodium naphthalenide addition. The reaction mixture was allowed to stir at room temperature for 2 h

after which THF was removed in vacuum. The crude product was redissolved in toluene and filtered. Slow diffusion of pentane into the toluene solution at -35 °C furnishes colorless crystals. The product was collected by filtration and washed three times with cold pentane. (Yield: 32 mg, 31%, two crops). ^{1}H NMR (400 MHz, C_6D_6; δ, ppm) at 65 °C: 7.40 (br, 4H, Ph*H*), 7.01 (br, 6H, Ph*H*), 6.78 (br, 4H, Ph*H*), 6.10 (br, 4H, Ph*H*), 2.42 (br, 12H, NCH_3). The broadening in the spectrum can be attributed to restricted rotation around the newly formed C-C bond. Single crystals suitable for X-ray crystallographic analysis were grown by slow diffusion of pentane into a saturated solution of (^{H}BI)$_2$ in toluene at -35 °C. Anal. Calcd for $C_{30}H_{30}N_4$: C, 80.68; H, 6.77; N, 12.55; Found: C, 80.72; H, 6.93; N, 12.27.

Associated Content

Supporting Information

Additional experimental procedures, spectroscopic data, crystallographic data for [Na(18-crown-6)(thf)$_2$][Zr(^{Me}PDP)$_2$]·3THF and (^{H}BI)$_2$, and computational details. The Supporting Information is available free of charge on the ACS Publications website.

Author Information

Corresponding Author

camilsmann@mail.wvu.edu

Notes

The authors declare no competing financial interest.

Acknowledgements

West Virginia University and the Don and Linda Brodie Resource Fund for Innovation are acknowledged for financial support. This work used X-ray crystallography (CHE-1336071) and NMR (CHE-1228336) equipment funded by the National Science Foundation. The WVU High Performance Computing facilities are funded by the National Science Foundation EPSCoR Research Infrastructure Improvement Cooperative Agreement #1003907, the state of West Virginia (WVEPSCoR via the Higher Education Policy Commission), the WVU Research Corporation, and faculty investments. The authors would like to thank Prof. Greg Scholes (Princeton University) for providing access to his group's time-resolved emission spectrometer.

References

(1) Small, B. L. *Acc. Chem. Res.* **2015**, *48*, 2599.

(2) Klosin, J.; Fontaine, P. P.; Figueroa, R. *Acc. Chem. Res.* **2015**, *48*, 2004.

(3) Chirik, P. J. *Acc. Chem. Res.* **2015**, *48*, 1687.

(4) McNeill, E.; Ritter, T. *Acc. Chem. Res.* **2015**, *48*, 2330.

(5) Greenhalgh, M. D.; Jones, A. S.; Thomas, S. P. *ChemCatChem* **2015**, *7*, 190.

(6) Friedfeld, M. R.; Shevlin, M.; Hoyt, J. M.; Krska, S. W.; Tudge, M. T.; Chirik, P. J. *Science* **2013**, *342*, 1076.

(7) Docherty, J. H.; Peng, J.; Dominey, A. P.; Thomas, S. P. *Nat. Chem.* **2017**, *9*, 595.

(8) Dawson, D. D.; Jarvo, E. R. *Org. Process Res. Dev.* **2015**, *19*, 1356.

(9) Jackson, E. P.; Malik, H. A.; Sormunen, G. J.; Baxter, R. D.; Liu, P.; Wang, H.; Shareef, A. R.; Montgomery, J. *Acc. Chem. Res.* **2015**, *48*, 1736.

(10) Tobisu, M.; Chatani, N. *Acc. Chem. Res.* **2015**, *48*, 1717.

(11) Bedford, R. B. *Acc. Chem. Res.* **2015**, *48*, 1485.

(12) Weix, D. J. *Acc. Chem. Res.* **2015**, *48*, 1767.

(13) Su, B.; Cao, Z. C.; Shi, Z. J. *Acc. Chem. Res.* **2015**, *48*, 886.

(14) Obligacion, J. V.; Semproni, S. P.; Chirik, P. J. *J. Am. Chem. Soc.* **2014**, *136*, 4133.

(15) Palmer, W. N.; Obligacion, J. V.; Pappas, I.; Chirik, P. J. *J. Am. Chem. Soc.* **2016**, *138*, 766.

(16) Toutov, A. A.; Liu, W. B.; Betz, K. N.; Fedorov, A.; Stoltz, B. M.; Grubbs, R. H. *Nature* **2015**, *518*, 80.

(17) Balzani, V.; Juris, A. *Coord. Chem. Rev.* **2001**, *211*, 97.

(18) Kalyanasundaram, K. *Coord. Chem. Rev.* **1982**, *46*, 159.

(19) Juris, A.; Balzani, V.; Barigelletti, F.; Campagna, S.; Belser, P.; von Zelewsky, A. *Coord. Chem. Rev.* **1988**, *84*, 85.

(20) Yeh, A. T.; Shank, C. V; McCusker, J. K. *Science* **2000**, *289*, 935.

(21) King, K. A.; Spellane, P. J.; Watts, R. J. *J. Am. Chem. Soc.* **1985**, *107*, 1431.

(22) Dixon, I. M.; Collin, J.-P.; Sauvage, J.-P.; Flamigni, L.; Encinas, S.; Barigelletti, F. *Chem. Soc. Rev.* **2000**, *29*, 385.

(23) Sato, S.; Matubara, Y.; Koike, K.; Katayama, T.; Ishibashi, Y.; Miyasaka, H.; Taniguchi, S.; Chosrowjan, H.; Mataga, N.; Fukazawa, N.; Koshihara, S.; Onda, K.; Ishitani, O. *Chem. Eur. J.* **2012**, *18*, 15722.

(24) Nahhas, A. El; Consani, C.; Blanco-Rodríguez, A. M.; Lancaster, K. M.; Braem, O.; Cannizzo, A.; Towrie, M.; Clark, I. P.; Stanislav, Z. *Inorg. Chem.* **2011**, *50*, 2932.

(25) Larsen, C. B.; Wenger, O. S. *Chem. Eur. J.* **2018**, *24*, 2039.

(26) Chábera, P.; Liu, Y.; Prakash, O.; Thyrhaug, E.; Nahhas, A. El; Honarfar, A.; Essén, S.; Fredin, L. A.; Harlang, T. C. B.; Kjær, K. S.; Handrup, K.; Ericson, F.; Tatsuno, H.; Morgan, K.; Schnadt, J.; Häggström, L.; Ericsson, T.; Sobkowiak, A.; Lidin, S.; Huang, P.; Styring, S.; Uhlig, J.; Bendix, J.; Lomoth, R.; Sundström, V.; Persson, P.; Wärnmark, K. *Nature* **2017**, *543*, 695.

(27) Lewis, N. S.; Nocera, D. G. *Proc. Natl. Acad. Sci.* **2006**, *103*, 15729.

(28) Crabtree, G. W.; Lewis, N. S. *Phys. Today* **2007**, *60*, 37.

(29) Balzani, V.; Credi, A.; Venturi, M. *ChemSusChem* **2008**, *1*, 26.

(30) Angnes, R. A.; Li, Z.; Correia, C. R. D.; Hammond, G. B. *Org. Biomol. Chem.* **2015**, *13*, 9152.

(31) Prier, C. K.; Rankic, D. A.; MacMillan, D. W. C. *Chem. Rev.* **2013**, *113*, 5322.

(32) Tucker, J. W.; Stephenson, C. R. J. *J. Org. Chem.* **2012**, *77*, 1617.

(33) Zeitler, K. *Angew. Chemie - Int. Ed.* **2009**, *48*, 9785.

(34) Xuan, J.; Xiao, W.-J. *Angew. Chemie - Int. Ed.* **2012**, *51*, 6828.

(35) Romero, N. A.; Nicewicz, D. A. *Chem. Rev.* **2016**, *116*, 10075.

(36) Greenwood, N. N.; Earnshaw, A. *Chemistry of the Elements - Second Edition*; Elsevier: Oxford, 1998.

(37) Yaroshevsky, A. A. *Geochemistry Int.* **2006**, *44*, 48.

(38) Arias-Rotondo, D. M.; McCusker, J. K. *Chem. Soc. Rev.* **2016**, *45*, 5803.

(39) Juban, E. A.; Smeigh, A. L.; Monat, J. E.; McCusker, J. K. *Coord. Chem. Rev.* **2006**, *250*,

1783.

(40) Fatur, S. M.; Shepard, S. G.; Higgins, R. F.; Shores, M. P.; Damrauer, N. H. *J. Am. Chem. Soc.* **2017**, *139*, 4493.

(41) Harlang, T. C. B.; Liu, Y.; Gordivska, O.; Fredin, L. A.; Ponseca, C. S.; Huang, P.; Chábera, P.; Kjaer, K. S.; Mateos, H.; Uhlig, J.; Lomoth, R.; Wallenberg, R.; Styring, S.; Persson, P.; Sundström, V.; Wärnmark, K. *Nat. Chem.* **2015**, *7*, 883.

(42) Monat, J. E.; McCusker, J. K. *J. Am. Chem. Soc.* **2000**, *122*, 4092.

(43) Duchanois, T.; Etienne, T.; Cebrián, C.; Liu, L.; Monari, A.; Beley, M.; Assfeld, X.; Haacke, S.; Gros, P. C. *Eur. J. Inorg. Chem.* **2015**, *2015*, 2469.

(44) Pirtsch, M.; Paria, S.; Matsuno, T.; Isobe, H.; Reiser, O. *Chem. Eur. J.* **2012**, *18*, 7336.

(45) Mara, M. W.; Fransted, K. A.; Chen, L. X. *Coord. Chem. Rev.* **2015**, *282–283*, 2.

(46) Cunningham, C. T.; Cunningham, K. L. H.; Michalec, J. F.; Mcmillin, D. R. *Inorg. Chem.* **1999**, *38*, 4388.

(47) McMillin, D. R.; Buckner, M. T.; Ahn, B. T. *Inorg. Chem.* **1977**, *16*, 943.

(48) Harkins, S. B.; Peters, J. C. *J. Am. Chem. Soc.* **2005**, *127*, 2030.

(49) Khnayzer, R. S.; McCusker, C. E.; Olaiya, B. S.; Castellano, F. N. *J. Am. Chem. Soc.* **2013**, *135*, 14068.

(50) McCusker, C. E.; Castellano, F. N. *Inorg. Chem.* **2013**, *52*, 8114.

(51) Büldt, L. A.; Wenger, O. S. *Angew. Chemie - Int. Ed.* **2017**, *56*, 5676.

(52) Sattler, W.; Henling, L. M.; Winkler, J. R.; Gray, H. B. *J. Am. Chem. Soc.* **2015**, *137*, 1198.

(53) Sattler, W.; Ener, M. E.; Blakemore, J. D.; Rachford, A. A.; Labeaume, P. J.; Thackeray, J. W.; Cameron, J. F.; Winkler, J. R.; Gray, H. B. *J. Am. Chem. Soc.* **2013**, *135*, 10614.

(54) Büldt, L. A.; Guo, X.; Prescimone, A.; Wenger, O. S. *Angew. Chemie - Int. Ed.* **2016**, *55*, 11247.

(55) Büldt, L. A.; Guo, X.; Vogel, R.; Prescimone, A.; Wenger, O. S. *J. Am. Chem. Soc.* **2017**, *139*, 985.

(56) *Transition Metal and Rare Earth Chemistry - Excited States, Transitions, Interactions I*; Yersin, H., Ed.; Springer, 2001.

(57) Yin, H.; Carroll, P. J.; Anna, J. M.; Schelter, E. J. *J. Am. Chem. Soc.* **2015**, *137*, 9234.

(58) Yin, H.; Carroll, P. J.; Manor, B. C.; Anna, J. M.; Schelter, E. J. *J. Am. Chem. Soc.* **2016**, *138*, 5984.

(59) Yin, H.; Jin, Y.; Hertzog, J. E.; Mullane, K. C.; Carroll, P. J.; Manor, B. C.; Anna, J. M.; Schelter, E. J. *J. Am. Chem. Soc.* **2016**, *138*, 16266.

(60) Qiao, Y.; Sergentu, D.-C.; Yin, H.; Zabula, A. V.; Cheisson, T.; McSkimming, A.; Manor, B. C.; Carroll, P. J.; Anna, J. M.; Autschbach, J.; Schelter, E. J. *J. Am. Chem. Soc.* **2018**, DOI:10.1021/jacs.7b13339.

(61) Guo, J. J.; Hu, A.; Chen, Y.; Sun, J.; Tang, H.; Zuo, Z. *Angew. Chemie - Int. Ed.* **2016**, *55*, 15319.

(62) Hu, A.; Guo, J.-J.; Pan, H.; Tang, H.; Gao, Z.; Zuo, Z. *J. Am. Chem. Soc.* **2018**, *140*, 1612.

(63) Suzuki, K.; Tang, F.; Kikukawa, Y.; Yamaguchi, K.; Mizuno, N. *Angew. Chemie - Int. Ed.* **2014**, *53*, 5356.

(64) Jenks, T. C.; Bailey, M. D.; Hovey, J. L.; Fernando, S.; Basnayake, G.; Cross, M. E.; Li, W.; Allen, M. J. *Chem. Sci.* **2018**, *9*, 1273.

(65) Pfennig, B. W.; Thompson, M. E.; Bocarsly, A. B. *J. Am. Chem. Soc.* **1989**, *111*, 8947.

(66) Pfennig, B. W.; Thompson, M. E.; Bocarsly, A. B. *Organometallics* **1993**, *12*, 649.

(67) Loukova, G. V.; Vasiliev, V. P.; Milov, A. A.; Smirnov, V. A.; Minkin, V. I. *J. Photochem. Photobiol. A Chem.* **2016**, *327*, 6.

(68) Loukova, G. V.; Starodubova, S. E.; Smirnov, V. A. *J. Phys. Chem. A* **2007**, *111*, 10928.

(69) Loukova, G. V.; Huhn, W.; Vasiliev, V. P.; Smirnov, V. A. *J. Phys. Chem. A* **2007**, *111*, 4117.

(70) Loukova, G. V.; Smirnov, V. A. *Chem. Phys. Lett.* **2000**, *329*, 437.

(71) Loukova, G. V. *Chem. Phys. Lett.* **2002**, *353*, 244.

(72) Heinselman, K. S.; Hopkins, M. D. *J. Am. Chem. Soc.* **1995**, *117*, 12340.

(73) Romain, C.; Choua, S.; Collin, J. P.; Heinrich, M.; Bailly, C.; Karmazin-Brelot, L.; Bellemin-Laponnaz, S.; Dagorne, S. *Inorg. Chem.* **2014**, *53*, 7371.

(74) Pritchard, V. E.; Thorp-Greenwood, F. L.; Balasingham, R. G.; Williams, C. F.; Kariuki, B. M.; Platts, J. A.; Hallett, A. J.; Coogan, M. P. *Organometallics* **2013**, *32*, 3566.

(75) Paulson, S.; Sullivan, B. P.; Caspar, J. V. *J. Am. Chem. Soc.* **1992**, *114*, 6905.

(76) Thorn, D. L.; Harlow, R. L. *Inorg. Chem.* **1992**, *31*, 3917.

(77) Gazi, S.; Hung Ng, W. K.; Ganguly, R.; Putra Moeljadi, A. M.; Hirao, H.; Soo, H. Sen. *Chem. Sci.* **2015**, *6*, 7130.

(78) Zhang, Y.; Petersen, J. L.; Milsmann, C. *J. Am. Chem. Soc.* **2016**, *138*, 13115.

(79) Zhu, X.-Q.; Zhang, M.-T.; Yu, A.; Wang, C.-H.; Cheng, J.-P. *J. Am. Chem. Soc.* **2008**, *130*, 2501.

(80) Kaljurand, I.; Kütt, A.; Sooväli, L.; Rodima, T.; Mäemets, V.; Leito, I.; Koppel, I. A. *J. Org. Chem.* **2005**, *70*, 1019.

(81) Cismesia, M. A.; Yoon, T. P. *Chem. Sci.* **2015**, *6*, 5426.

(82) McDaniel, A. M.; Tseng, H. W.; Damrauer, N. H.; Shores, M. P. *Inorg. Chem.* **2010**, *49*, 7981.

(83) Stevenson, S. M.; Shores, M. P.; Ferreira, E. M. *Angew. Chemie - Int. Ed.* **2015**, *54*, 6506.

(84) Darwent, J. R.; Douglas, P.; Harriman, A.; Porter, G.; Richoux, M.-C. *Coord. Chem. Rev.* **1982**, *44*, 83.

(85) Neese, F. *J. Biol. Inorg. Chem.* **2006**, *11*, 702.

(86) Klamt, A.; Schürmann, G. *J. Chem. Soc. Perkin Trans. II* **1993**, 799.

(87) Connelly, N. G.; Geiger, W. E. *Chem. Rev.* **1996**, *96*, 877.

(88) Gowda, A. S.; Petersen, J. L.; Milsmann, C. *Inorg. Chem.* **2018**, *57*, 1919.

(89) Lu, C. C.; Bill, E.; Weyhermüller, T.; Bothe, E.; Wieghardt, K. *J. Am. Chem. Soc.* **2008**, *130*, 3181.

(90) Zhang, S.; Naab, B. D.; Jucov, E. V.; Parkin, S.; Evans, E. G. B.; Millhauser, G. L.; Timofeeva, T. V.; Risko, C.; Brédas, J. L.; Bao, Z.; Barlow, S.; Marder, S. R. *Chem. Eur. J.* **2015**, *21*, 10878.

(91) Naab, B. D.; Zhang, S.; Vandewal, K.; Salleo, A.; Barlow, S.; Marder, S. R.; Bao, Z. *Adv. Mater.* **2014**, *26*, 4268.

(92) Yasu, Y.; Koike, T.; Akita, M. *Adv. Synth. Catal.* **2012**, *354*, 3414.

(93) Janzen, E. G. *J. Magn. Reson.* **1973**, *9*, 510.

(94) Park, G.; Yi, S. Y.; Jung, J.; Cho, E. J.; You, Y. *Chem. Eur. J.* **2016**, *22*, 17790.

Table of Contents Graphic

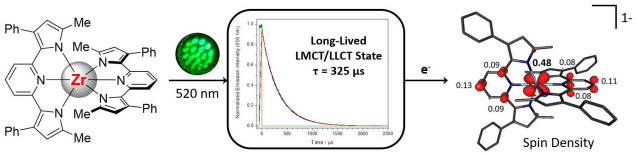

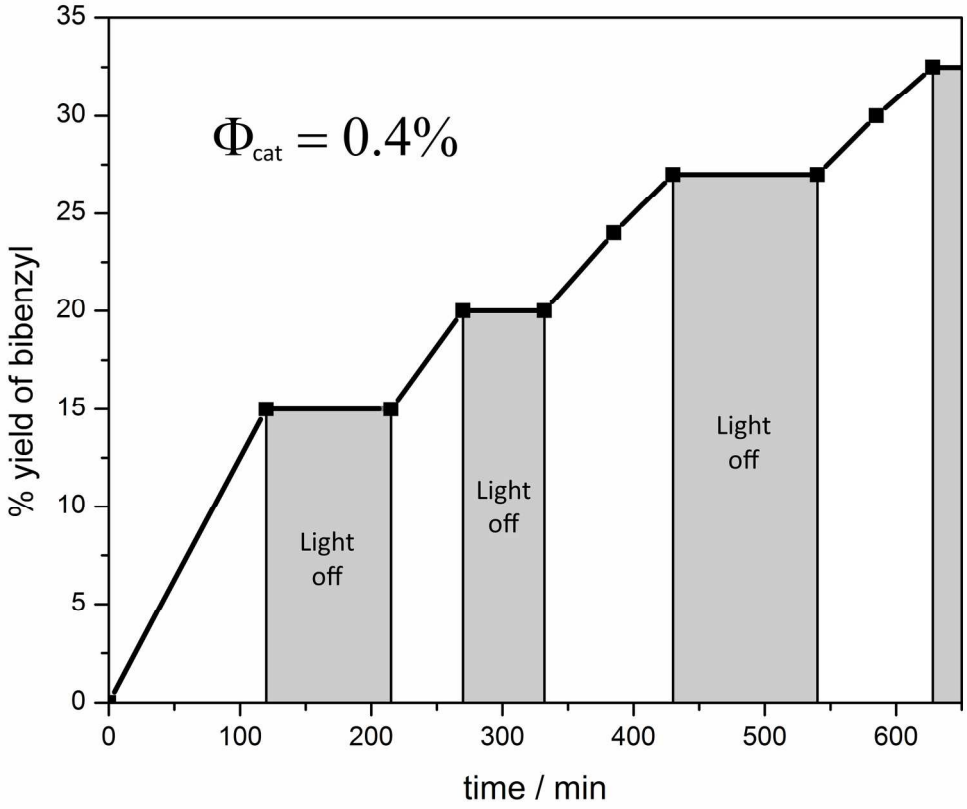

179x148mm (300 x 300 DPI)

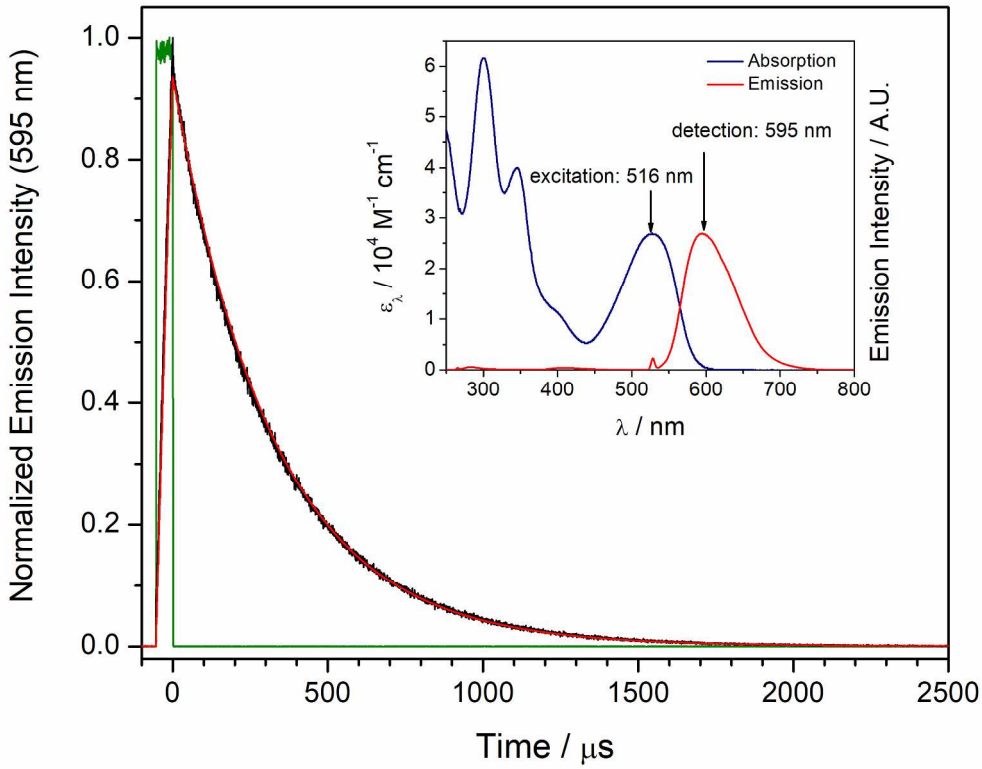

228x178mm (300 x 300 DPI)

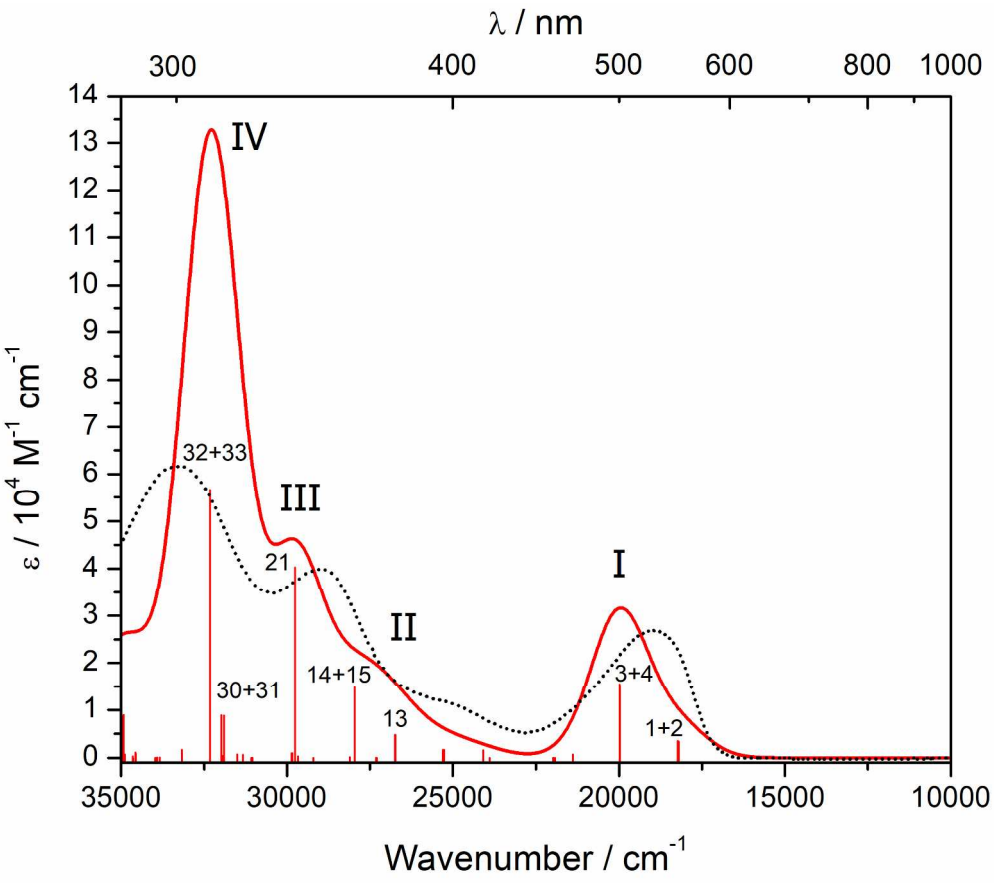

223x196mm (300 x 300 DPI)

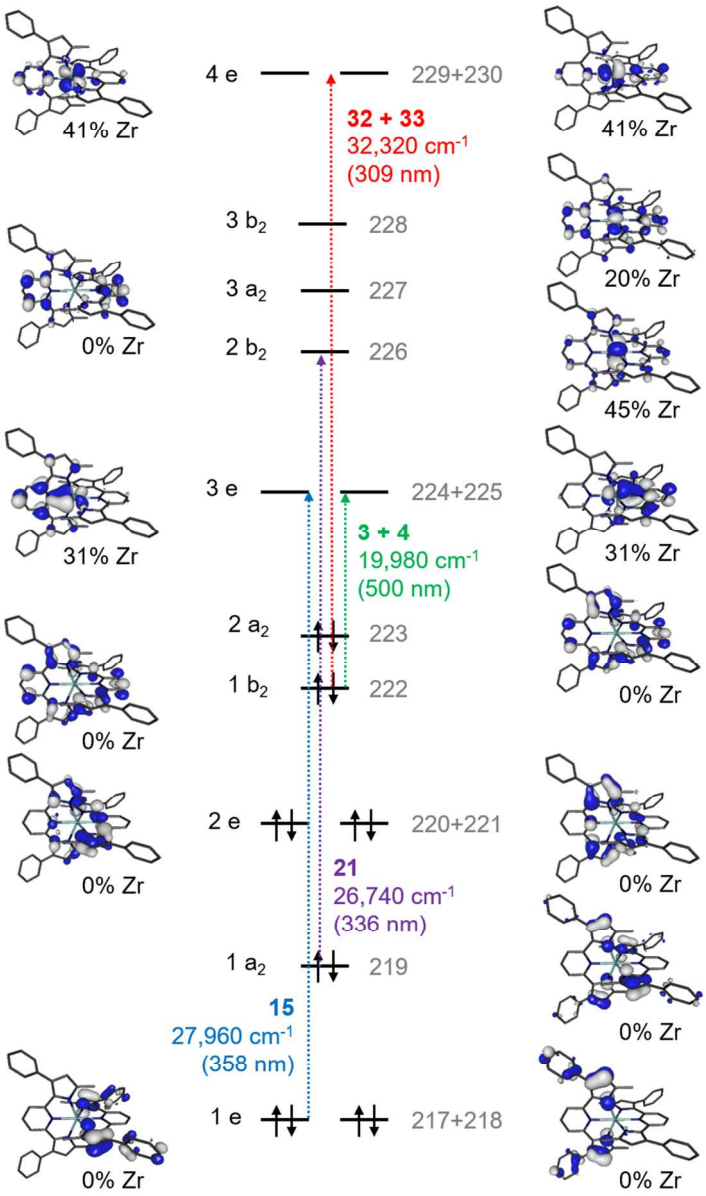

154x253mm (150 x 150 DPI)

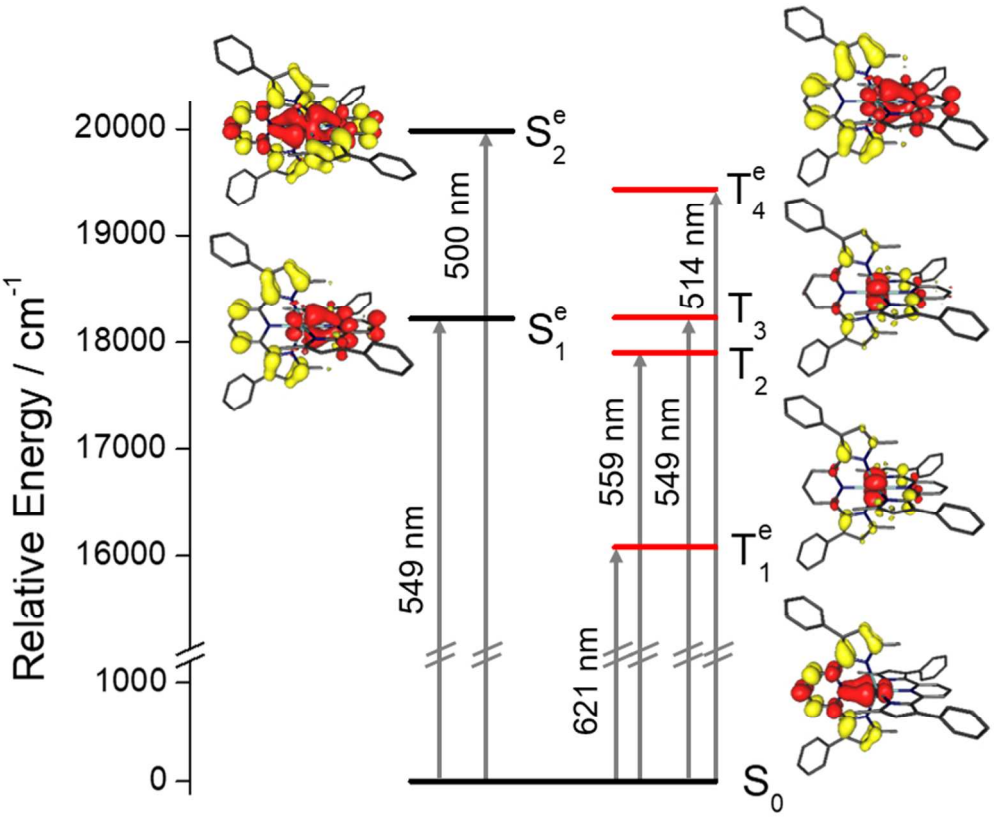

149x122mm (150 x 150 DPI)

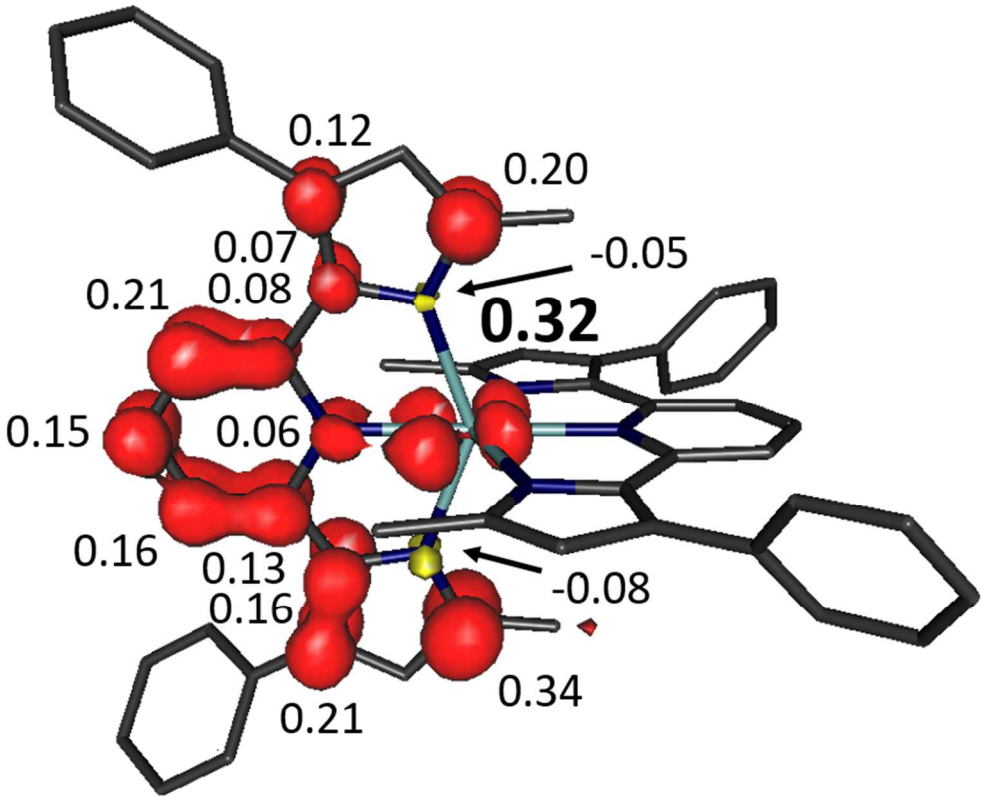

146x119mm (150 x 150 DPI)

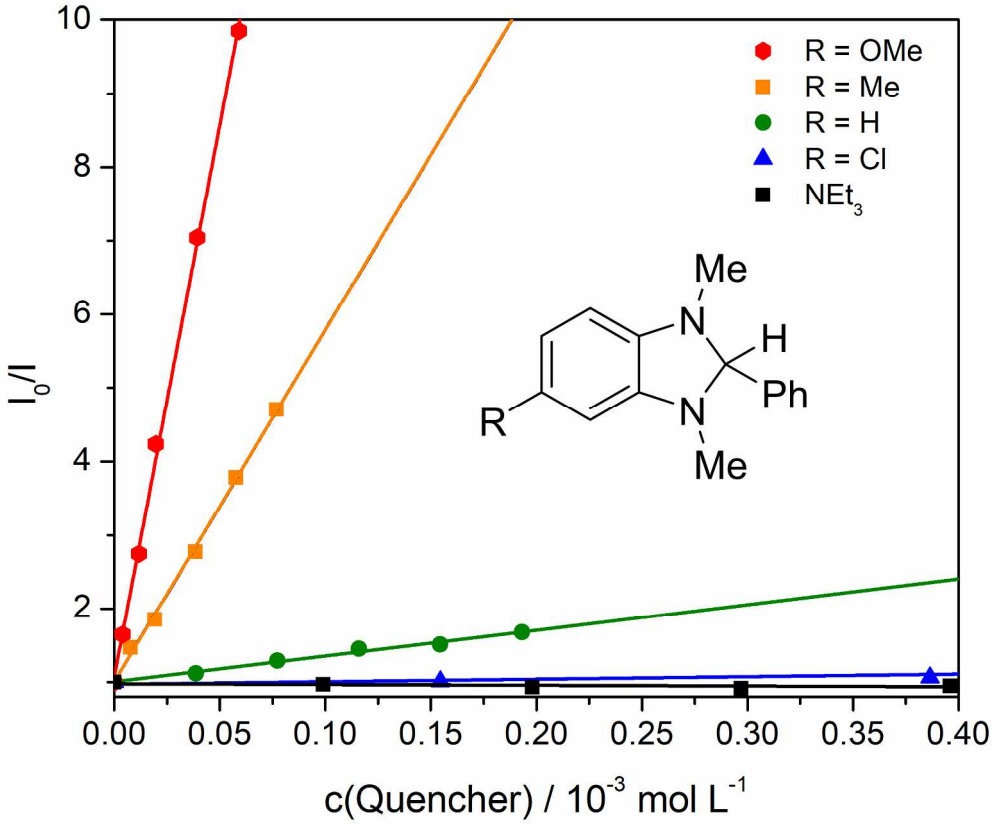

219x183mm (300 x 300 DPI)

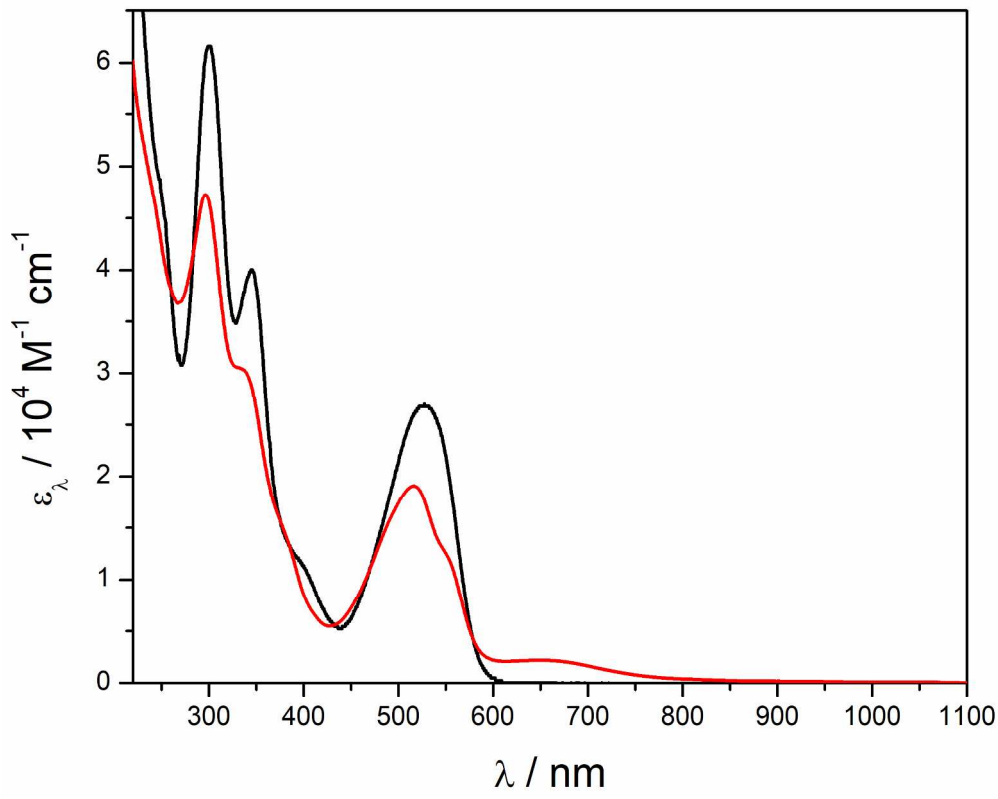

221x177mm (300 x 300 DPI)

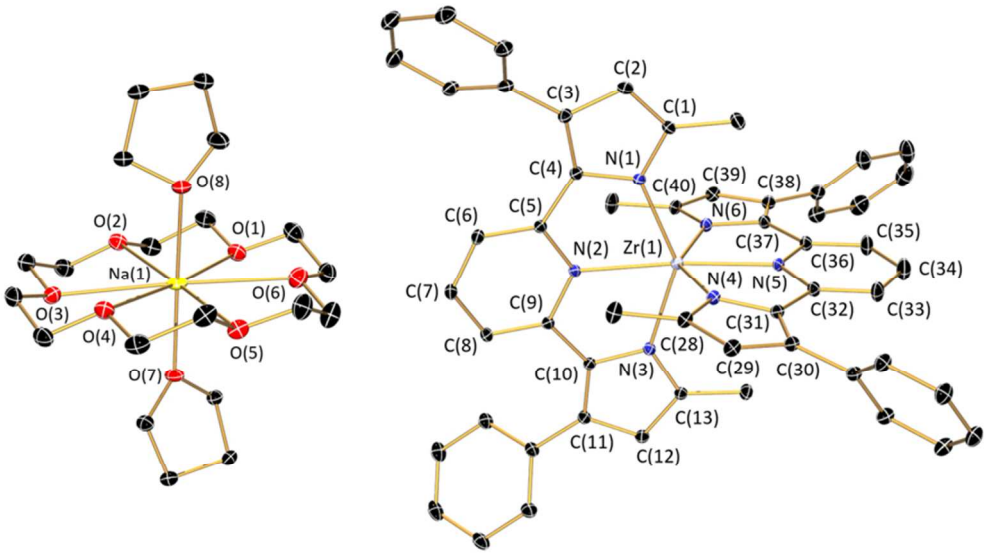

150x84mm (150 x 150 DPI)

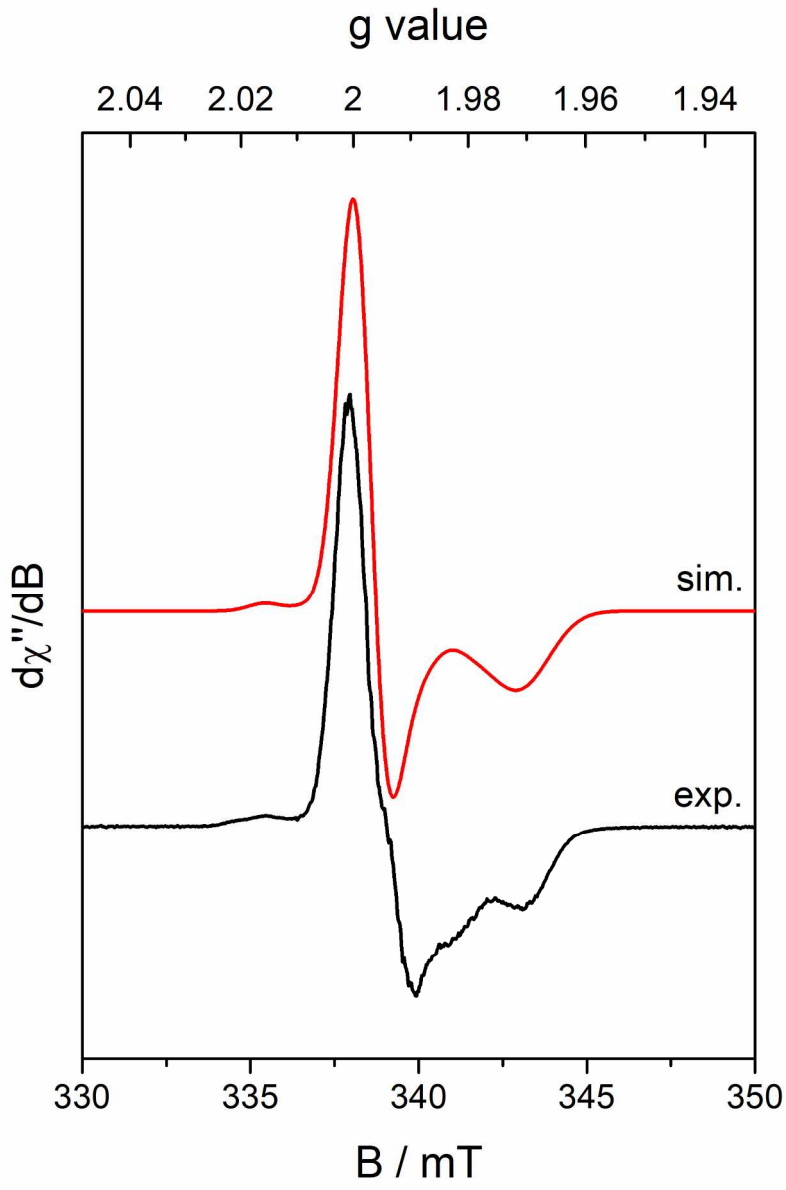

169x252mm (300 x 300 DPI)

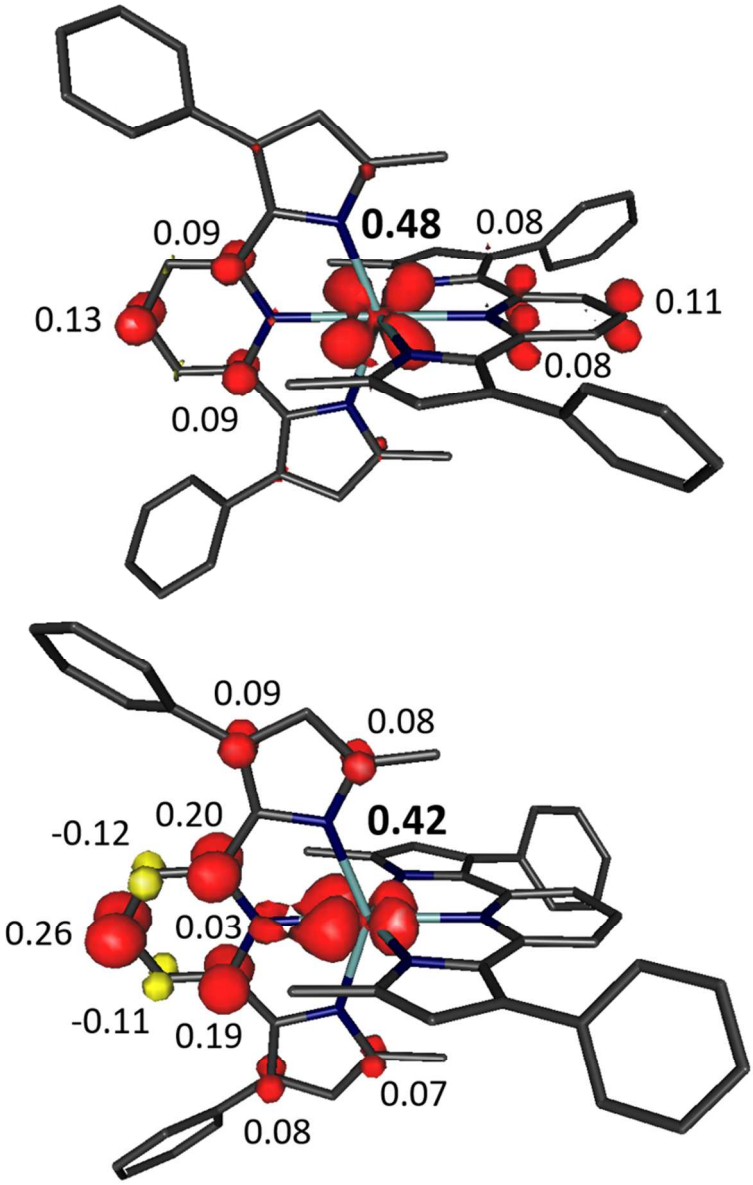

136x210mm (150 x 150 DPI)

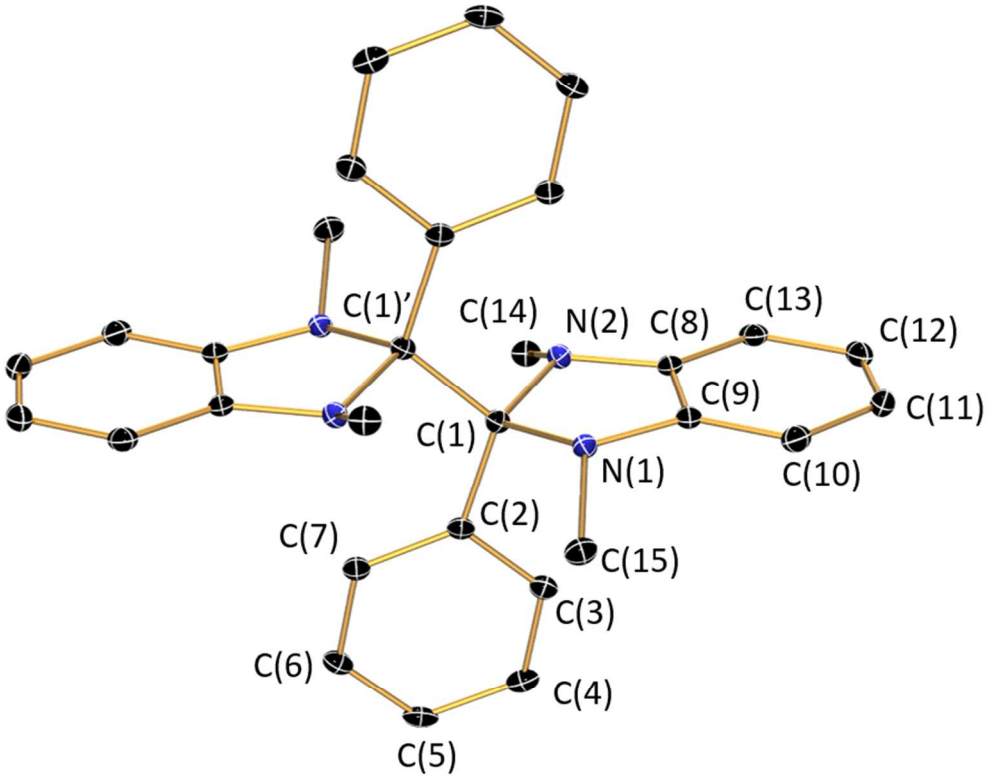

152x122mm (150 x 150 DPI)

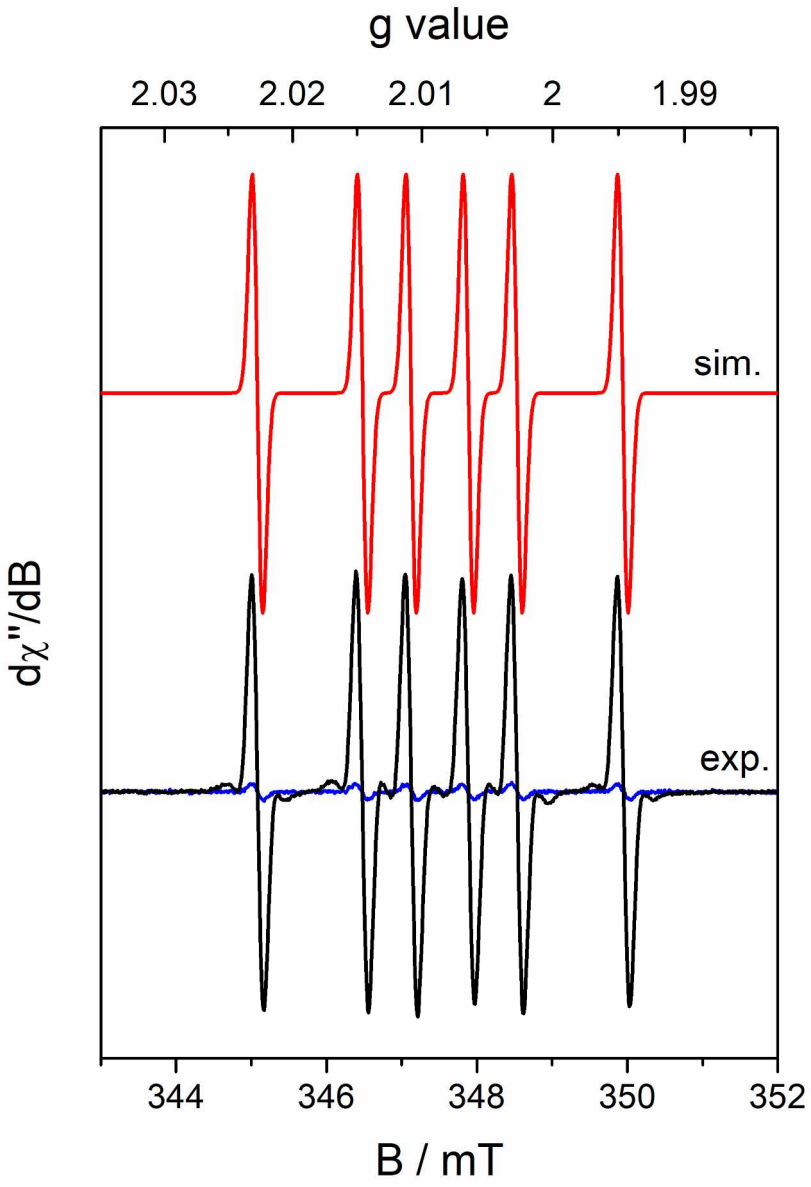

175x250mm (300 x 300 DPI)